UNIVERSIDADE DA CORUÑA

FACULTAD DE CIENCIAS

Chemistry Degree

Degree dissertation

SYNTHESIS AND CHARACTERIZATION OF PHOTOVOLTAIC MATERIALS FOR LOW COST AND HIGH EFFICIENCY SOLAR PANELS

SÍNTESE E CARACTERIZACIÓN DE MATERIAIS FOTOVOLTAICOS PARA PANEIS SOLARES DE BAIXO CUSTE E ALTA EFICIENCIA

SÍNTESIS Y CARACTERIZACIÓN DE MATERIALES FOTOVOLTÁICOS PARA PANELES SOLARES DE BAJO COSTE Y ALTA EFICIENCIA

Directors: **Manuel Sánchez Andujar**
Socorro Castro García

FERNÁN GARCÍA GONZÁLEZ

Term: 2014/2015 – Call: September

“The consciousness of AC encompassed all of what had once been a Universe and brooded over what was now Chaos. Step by step, it must be done.

And AC said, “LET THERE BE LIGHT!”

And there was light…”

The Last Question
Isaac Asimov

INDEX

1 ABSTRACT

1.1 English

This dissertation studies the use of the hybrid perovskite $(CH_3)_2NH_2PbI_3$ in solid-state dye sensitized solar cells (ssDSSC), which was not previously described in the literature. To that end, thin films of the perovskite were prepared using both the one-step spin-coating and the two-step spin-coating techniques. Those films were characterized by XR powder diffraction and scanning electron microscopy. Furthermore, the UV-Vis spectrum of the compound was obtained, as well as its band gap and structure.

The UV-visible absorption spectrum of the $(CH_3)_2NH_2PbI_3$ revealed that it absorbed only in the blue region and the ultraviolet zone, while its band gap was 2.81 eV. Although these optical properties are not adequate for photovoltaic applications, they it make an interesting candidate for use in a blue LED design. The structure of the compound is that of a hexagonal perovskite, due to the big size of the dimethlyammonium cation.

At first, a non-homogenous layer of $(CH_3)_2NH_2PbI_3$ was deposited, with a needle-like structure, and which was due to a large particle size of the precursor solutions. The particle size of the solutions was proved to be in relationship with the amount of organic compounds present in the solution, as it was reduced adding MAX or DMAX as additives (methyl or dimethlylammonium halides, where X is either Cl^- or I^-).

Also, this memory reports the influence of the additives in the particle size of the colloids and in film morphology on hybrid perovskite $CH_3NH_3PbI_3$. The obtained results shown that methylammonium chloride employed as additive induces a reduction of particle size of the precursor solutions leading to better, more homogeneous morphologies.

1.2 Galego

Este traballo estuda o uso da perovskita híbrida $(CH_3)_2NH_2PbI_3$ en células solares sensitivizadas por colorantes de estado sólido (ssDSSC), a cal non fora descrito anteriormente na bibliografía. Para ese fin, capas finas da perovskita foron preparadas polos procedementos de spin-coating en un e dous pasos, respectivamente. Esas capas foron caracterizadas por difracción de raios-X en po e por microscopía electrónica de varrido. Ademais, o espectro de UV-Vis foi obtido, así como o seu bandgap e a súa estrutura.

O espectro de absorción de UV-visible do $(CH_3)_2NH_2PbI_3$ revelou que este solo absorbía na rexión ultravioleta, mentres que o seu band gap era 2.81 eV. Aínda que estas propiedades non eran adecuadas para aplicacións fotovoltaicas, tamén o fan un candidato interesante para o seu uso nun LED azul. A estrutura cristalina do composta é a dunha perovskita hexagonal, debido o gran tamaño do catión dimetilamonio.

Ao principio depositouse unha capa non homoxénea de $(CH_3)_2NH_2PbI_3$, cunha estrutura en forma de agullas, o calé debido ao gran tamaño de partícula das disolucións precursoras. Demostrouse que o tamaño de partícula das solución precursoras esta relacionado coa cantidade de compostos orgánicos presentes na disolución, xa que foi reducido ao engadir MAX ou DMAX como aditivos (haluros de metil o dimetil amonio, sendo X ben Cl^- ou I^-).

Esta memoria tamén reporta a influencia dos aditivos nos coloides e na morfoloxía das capas da perovskita híbrida $CH_3NH_3PbI_3$. Os resultados obtidos mostran que o emprego de cloruro de metilamonio como aditivo induce unha redución do tamaño de partícula das solución precursoras, levando á obtención de morfoloxías mellores e máis homoxéneas.

1.3 Castellano

Este trabajo estudia el uso de la perovskita hibrida $(CH_3)_2NH_2PbI_3$ en células solares sensitivizadas por colorantes de estado sólido (ssDSSC), el cual no había sido descrito anteriormente en la literatura. Para tal fin, capas finas de la perovskita se prepararon usando las técnicas de spin-coating en uno y dos pasos. Esas capas fueron caracterizadas por difracción de polvo de rayos-X y por microscopía electrónica de barrido. Además, se obtuvo el espectro UV-Vis del compuesto, así como su band gap y su estructura.

El espectro de absorción de UV-Vis del $(CH_3)_2NH_2PbI_3$ reveló que solo absorbe en la zona azul y la ultravioleta, mientras que su band gap es de 2.81 eV. Aunque estas propiedades no son adecuadas para aplicaciones fotovoltaicas, hacen del compuesto un candidato interesante para su uso en un LED azul. La estructura cristalina del compuesto es la de una perovskita hexagonal, debido al gran tamaño del ion central.

Al principio se depositó una capa no homogénea de $(CH_3)_2NH_2PbI_3$, con una estructura en forma de agujas, y que es debida al gran tamaño de partícula de la disoluciones precursoras. El tamaño de partícula de las disoluciones, a su vez, se demostró que está relacionado con la cantidad de compuestos orgánicos presentes en la muestra, ya que se redujo al añadir MAX o DMAX como aditivos (haluros de metil o dimetil amonio, siendo X bien Cl^- o I^-).

Asimismo, esta memoria reporta la influencia de los aditivos en el tamaño de partícula de los colides, así como en la morfología de las capas de perovskita híbrida $CH_3NH_3PbI_3$. Los resultados obtenidos muestran que el uso de cloruro de metilamonio como aditivos induce una reducción del tamaño de partícula de las disoluciones precursoras, llevando a la obtención de morfologías mejores y más homogéneas.

2 INTRODUCTION

At this point, it has become almost a cliché to state the need for clean and renewable sources of energy. Nevertheless, the search to cover this need is probably one of the greatest challenges facing humanity in this century. The overreliance in non-renewable and polluting sources of energy, such as coal, natural gas and the infamous oil, has created a system that is not sustainable. Furthermore, the emission of greenhouse gases (CO_2 being the most famous) has provoked an anthropogenic climate chaos that jeopardizes not only the survival of countless species, but the means of living of many societies. All these are undisputable facts, with almost unanimous scientific consensus behind them[1], that need to be addressed. And while it is true that a successful response to climate change cannot only be technological in scope, science and technology still play a crucial part in overcoming this challenge. Ever since they saw widespread use, the solar cells have been put as an example of the clean and renewable energies needed for the future. However, many aspects still need to be improved: the current photovoltaic cells require high purity silicon, doped with several scarce elements, such as Gallium and Indium which greatly increase the price of the cells, as well as their availability. New research should focus in overcoming these issues, as well as improving performance, and the new solid-state dye sensitized solar cells show promising characteristics.

2.1 Photovoltaic cells[2]

Solar cell can be divided in those based in the technology of silicon semiconductors and those based in the dye sensitized solar cell technology. While this dissertation will focus on the second ones, it is still necessary to understand the silicon based solar cells, since they are the basis upon the technology is based. Furthermore they remain the benchmark against which all new cells are measured.

2.1.1 Electronic band theory[3]

To comprehend the photovoltaic effect, which is the basis for any solar cell, an understanding of the principles of semiconductors is vital. These materials, which form the basis of

much of modern technology, can be though as a middle ground between conductors, able to conduct electrical current with little resistance, and insulators, unable to do so. These properties can be explained through the electronic band theory.

The electronic band theory states that in any solid with a large number of atoms, *N*, the individual electronic states of the atoms begin to split into closely separated states, due to the interaction with other atoms. While at first an energy gap may exist between the individual electronic states, soon it becomes small enough to be able to talk about a continuous electron energy band. However, some energy levels may remain empty of electron energy bands, since no electronic state has those energies. These forbidden spaces usually form gaps between the different bands.

The number of states present in every band equals the number of states contributed by the *N* atoms of the solid; so an *s* band will have *N* states and a *p* band, *3N*. The number of electrons will also be equal to the number of electrons originally present in the isolated atoms. As a consequence, bands may be partially filled, or even empty of electrons. The energy of the highest filled state at 0 K is called the Fermi level, E_f. Different electron band structures are thus possible, as shown in **Figure 2.1**, and are as follows:

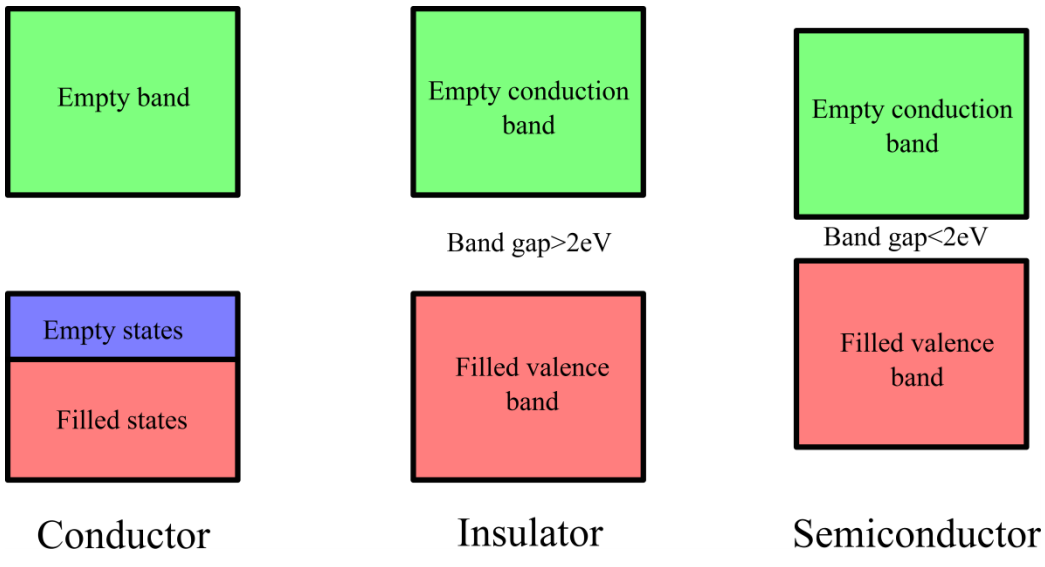

Figure 2.1

Electronic band structures of conductors, insulators and semiconductors

- Conductors: This is characteristic for metals, for which the number of possible states is greater than the number of valence electrons. As a result, the valence band is only partially filled, and the Fermi level is located within it.
- Insulator: For these materials the so-called valence band is completely filled; and the only empty states are located in the conduction band, which is completely empty. Both bands are separated by a large energy band gap, where the Fermi level is located. This band gap is usually greater than 2 eV.
- Semiconductors: Their structure is almost identically to an insulator, with a completely filled valence band and a completely empty conduction band. The energy band gap between them, however, is much smaller than in an insulator, less than 2 eV, and can be overcome by some electrons under the right circumstances.

Conduction of electrical current requires electrons to have energies larger than the Fermi level, becoming free electrons. In the case of conducting materials this is easily achieved. As shown before, the Fermi level is within the band itself, so the energy required to promote electrons above it is rather small. Usually, the energy coming from the electric field itself is more than enough. For insulators and semiconductors, however, the band gap lies between the highest filled state and the lowest empty state still above the Fermi level. To be able to conduct, an external source, such as light or temperature, must give the electrons enough energy to overcome the band-gap. In the case of insulators, the band gap is too large to be overcome by those sources, so they are not able to conduct under most circumstances. For semiconductors, however, the band gap is small enough to be overcome, promoting electrons from the valence band into the conduction band, where they become free electrons. Despite this, the conductivity of semiconductors will remain lower than that of the conductors, and be highly dependent on the temperature.

When an electron is promoted into the conduction band, an empty electronic state is left in the valence band. This empty state can be re-filled by other electrons, leaving another empty state in turn. Thus, it is convenient to treat a vacant state as a positively charged particle called a “hole”. This particle would have the same charge that the electron, only positive, and can also take part in the conduction of electrical current in semiconductors. If a hole

and a free electron meet, they will recombine, filling the empty vacant state. Both free electrons and holes are known collectively as charge carriers.

2.1.2 Extrinsic semiconductors

The semiconductors described above are intrinsic semiconductors, that is, their electronic properties depend only on their electronic band structure. However, most of the semiconductors employed nowadays are extrinsic semiconductors, where the electronic properties also depend on small impurities of other elements introduced to the material. This impurities need to be introduced with great care, in a process known as doping, since concentrations of just one atom in every 10^{12} Si atoms can turn silicon into a extrinsic semiconductor.

Depending on the nature of the doping elements, the extrinsic semiconductors are classified in *p*-type and *n*-type semiconductors. Both are schematized in **Figure 2.2**, and are as follows:

- *n*-type semiconductor: In this case, the silicon is doped with small amounts of an element with more valence electrons (such as P, As or Sb). Those extra electrons are located in the so-called donor states, situated just below the conduction band of the silicon. At room temperature, thermal energy is enough to promote some electrons from the donor states to the conduction band, where they become conducting free electrons. Since all free electrons come from the donor states (the intrinsic effects are usually negligible) no corresponding hole is formed in the valence band, thus all conductivity in *n*-type semiconductors is due to free electrons, and is a function of both temperature and donor concentration.

- *p*-type semiconductor: They are the opposite of the *n*-type semiconductors. They are doped with elements with less valence electrons than silicon (such as B, Al or Ga). Those elements introduce empty electron states just above the valence band, with low enough energy to accept electrons coming from the valence band, called acceptor states. The promoted electrons leave behind in the valence band positively charged holes that can conduct charge in an analogous way to the free electrons in the conduction band. Similarly, no free electrons are promoted to the conduction band, and conductivity is only due to the holes in the valence band.

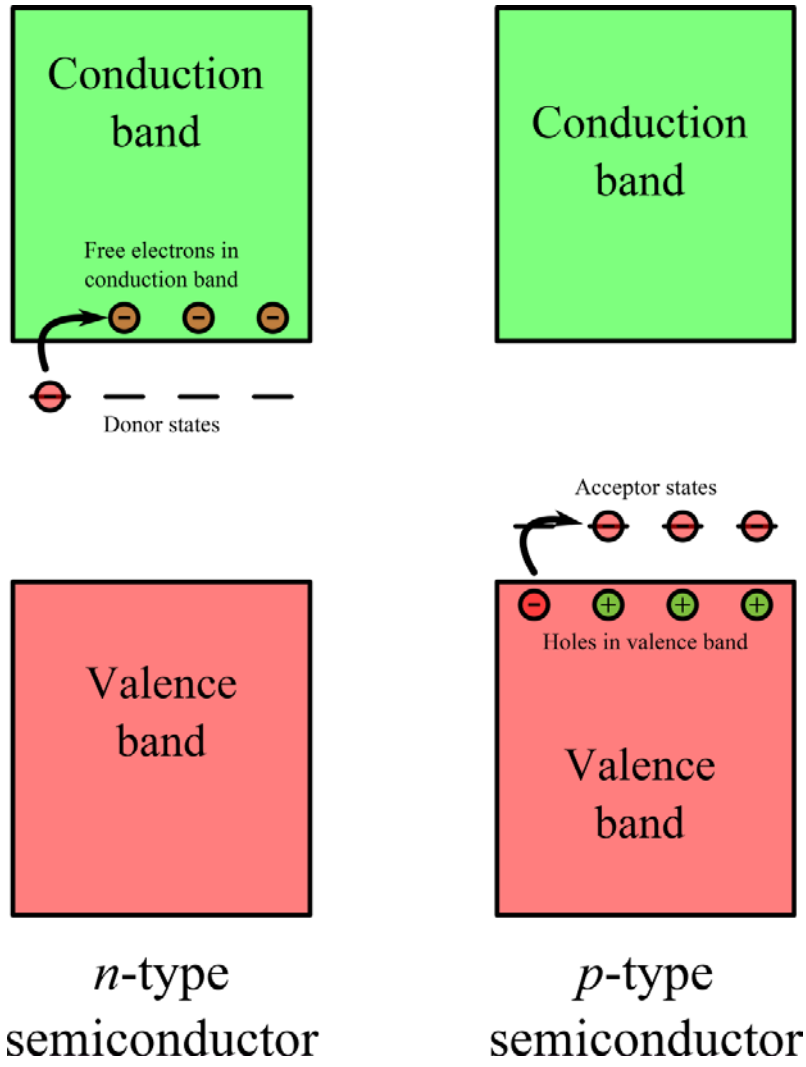

Figure 2.2

The two types of extrinsic semiconductors

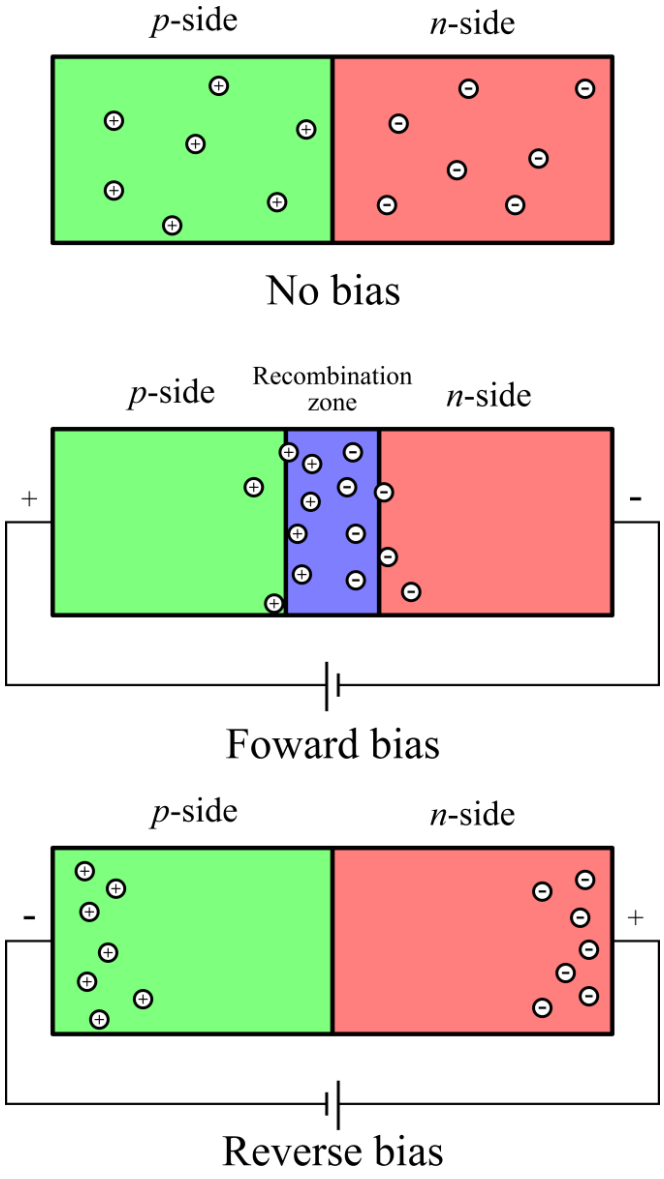

Figure 2.3

The three different bias of a diode

2.1.3 The p-n junction

The *p-n* junction, one way or another, is the basis of many current electronic devices. One of the most basic ones, but which exemplifies very well the principles behind the *p-n* junction is the diode, or a rectifier. It is a device that only allows the current to flow in a direction, and it is made from one piece of a semiconductor, doped in ones side to be a *p*-type and *n*- type in the other. This way, any external electrical potential can be established in two different ways: When the positive terminal of a battery is connected to the *p*-side and the negative terminal to the *n*-side, then it is referred as a forward bias. The opposite polarity is known as reverse bias. The three possibilities (no bias, forward bias and reverse bias) are represented in **Figure 2.3**.

- When no bias is present, both sides act as normal extrinsic semiconductors. In the *p*-side the majority of charge carriers are holes, while in the *n*-side they are electrons.
- When a forward bias is applied new electrons ae injected into the *n*-side, which flow to the junction. Similarly, holes in the *p*-side are also attracted to the junction. There; in the so called recombination, or depletion, zone; holes and electrons con-

tinually recombine and annihilate each other. Since there is a continuous flow of charge carriers, the electrical current can be conducted.

- When the reverse bias is applied both holes and repelled from the junction and no recombination takes place. The flow of charge carriers is interrupted and the diode becomes an insulator.

2.1.4 The silicon photovoltaic cell[4]

The principles explained above for the *p*-*n* junction also apply to the silicon photovoltaic cell. The basis of a photovoltaic cell is a *p*-*n* junction, in which the *p*-side is much thicker than the *n*-side. Because of that, most of the photons coming from sunlight are absorbed either in the recombination zone or in the *p*-side.

If the photon has an energy greater than the band-gap of the semiconductor (1.1 eV for Silicon), it is able to promote one electron from the valence band into the conduction band. Thus, an electron-hole pair (EHP) is generated. If the EHP was generated within a certain diffusion length, L_e for electrons and L_h for holes, then the electrons are able to diffuse

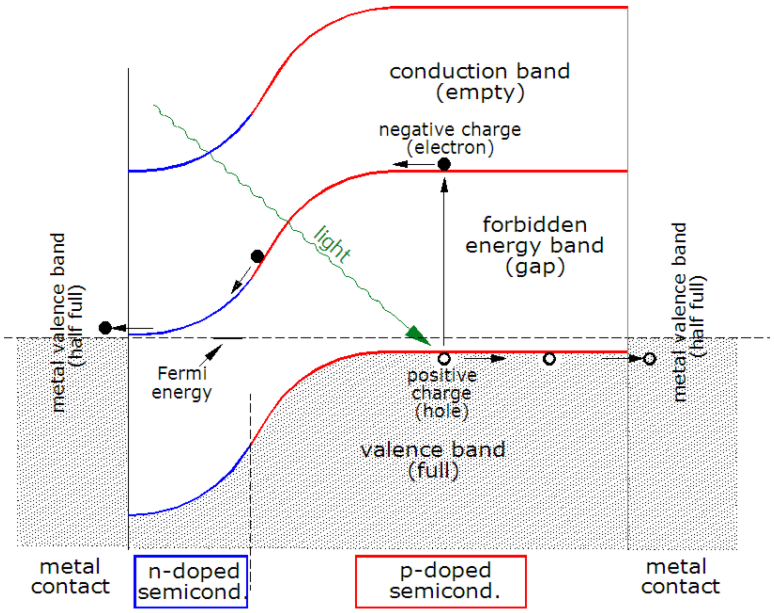

Figure 2.4

Electronic band diagram of a solar cell

back into the recombination zone. If the EHP is created outside those distances, then recombination will take place before any diffusion. The charge carriers that reach the junction are swept back into the *n*-side if they are electrons and into the *p*-side if they are holes. If an electrode is attached to each side, then an electrical current is generated. The whole process is summarized in **Figure 2.4**. There, the electronic bands of the solar cell are shown, as well as the energy path of the generated electron.

For obvious reasons, the band gap of the semiconductor is crucial to the performance of the solar cell. Small bandgaps are often more desirable, since less energy is required to promote electrons to the conduction band. However, the extra energy of photons above the band gap is usually lost in form of thermal, rather than electric, energy, lowering the efficiencies. It should be noted that, since most of the sunlight belongs either to the visible light or the near infrared, solar cells need to be optimized to work at those frequencies.

One way of trying to surpass the inherent limitations of conventional solar cell was the development of multijuction photocells, also known as tandem solar cells. These cells consist of several layers of semiconductors stacked in top of each other, each one with a different band gap. The top layer semiconductors, with higher band gaps, absorb higher energy photons; while the bottom semiconductors, with lower bad gaps, absorb the lower energy photons. This has allowed solar cell to achieve efficiencies never seen before. Another development of the silicon solar cell was the thin-film solar cell using amorphous silicon. The numerous grain boundaries lead to a higher band gap that more efficiently captures sunlight.

However, all silicon based solar cells face the same economic problems. They rely on a supply of high purity silicon, and while silicon is an abundant element, the necessary purification is an energy intensive process. Furthermore, the growing demand of silicon for use in solar cells conflicts with the also growing demand of silicon for use in electronic appliances. While there is undergoing research to produce solar-quality silicon in a cheaper way, they have yet to be successful[5]. Furthermore, almost all types of solar cells require quantities of Gallium and Indium, elements with a low concentration on the Earth's crust. Those

could become a dangerous bottleneck that could limit the expansion of the photovoltaic technology[6].

2.2 Dye sensitized solar cells[7]

To overcome the problems faced by the conventional, silicon based solar cells, a radically new approach began to take form in 1960's. Moving away from silicon based alternatives, a new type of solar cell was developed in which light absorption and charge generation took place in different devices. Since the light absorption originally took place in an organic dye, this type of cells came to be known as dye sensitized solar cells, DSSC.

2.2.1 Origins of the DSSC

While the first paper studying the possibilities of photoelectrochemical cell dates back to 1887[8], and by 1965 the first working cells had already been constructed[9]; it was only in 1991 when the first major breakthrough was achieved. Using a mesoporous TiO_2 film, O'Reagan and Grätzel were able to dramatically increase the surface area of the dye, leading to higher efficiency in the conversion of photons[10]. This mesoporous TiO_2 layer would become an integral part of all future designs, including solid-state DSSC (ssDSSC), until it was replaced by a compact layer of TiO_2 in the later perovskite based solar cells.

The basics of a DSSC cell are not dissimilar to those of the silicon solar cell: An electron-hole pair is formed by the absorbed energy of the photons; then, the charge carriers flow back to their respective electrodes, creating an electric current. Keeping these basics in mind is easy to understand the working of a DSSC, as shown in **Figure 2.5**[7], which consists of the following processes:

1. Excitation of the dye to a higher energy state by a photon.
2. Electron injection by the dye into the metal oxide (usually TiO_2).
3. Electron transport to the working electrode.
4. Excited-state decay of the dye.

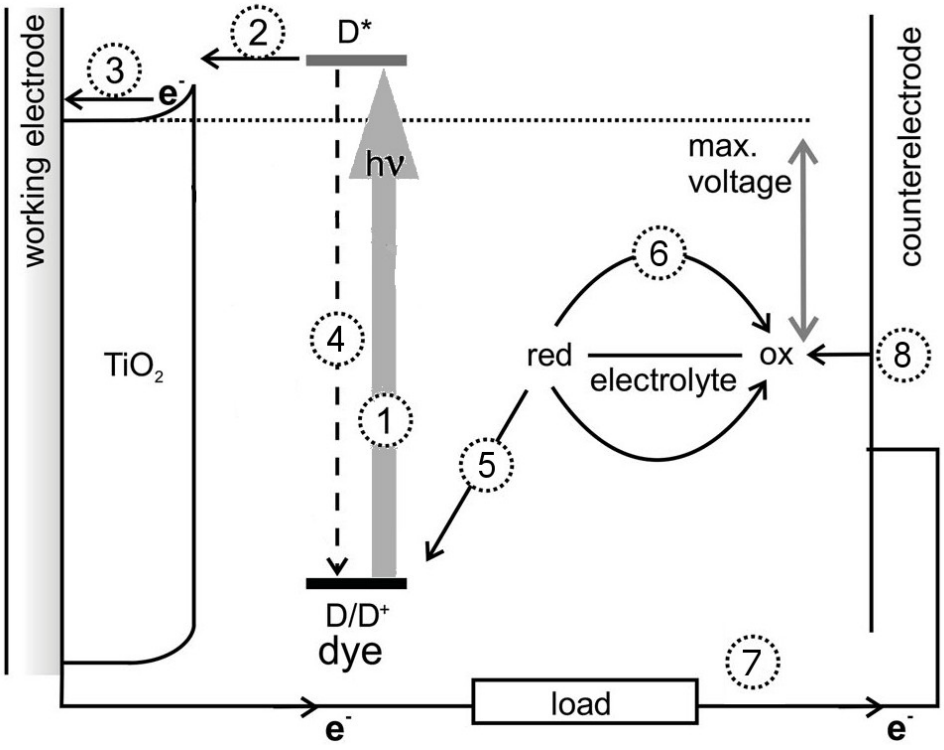

Figure 2.5

Schematized energy diagram of a DSSC[7]

5. Regeneration of the excited dye by electron transfer of the donor species.
6. Hole transport to the counterelectrode.
7. Transport of electrons from the working electrode to the counterelectrode, generating electrical current.
8. Regeneration of the oxidized donor.

The donor species is usually an $I_3^-/3I^-$ redox system in a liquid ionic electrolyte.

2.2.2 Solid-state DSSC

It was soon proved that the use of liquid electrolytes led to serious problems of corrosion, as well as hindering the true potential of the DSSC. This is due to the overpotential required to oxidize the electrolyte[11]. To mitigate those issues, it was attempted to exchange the liquid electrolyte and the I_3^- shuttle with some kind of solid hole-transporting material, or HTM. The first cell to achieve this was reported in 1998, and it used an amorphous organic

material; 2,2',7,7'-tetrakis(*N*,*N*-di-p-methoxyphenyl-amine)9,9'-spirobiflourene (spiro-OMeTAD); as the HTM[12]. Soon, all DSSC that did not use a liquid electrolyte were known as solid-state DSSC, or ssDSSC, and became the new front of research.

The new ssDSSC were not without their drawbacks, however. One crucial step to be resolved was to achieve a good pore filling of the TiO_2 layer by the dye[13]. Failure to this caused a limitation on the thickness of the cells at a level below the optical depth of the composite, causing a performance below the theoretical maximum. Several methods were tried to improve pore filling, and it remains one of the main challenges in the development of the ssDSSC.

Simultaneously, improvements to the organic dyes used in the original DSSC were also researched. Eventually, the possibility of employing *p*-type semiconductors as sensitizers was studied[14]. Inorganic sensitizers had high molar extinction coefficients, which led to better light absorption. Several materials were tried until the research led to the use of hybrid inorganic-organic perovskites, such as methylammonium lead iodide, $CH_3NH_3PbI_3$ ($MAPbI_3$), as sensitizer. $MAPbI_3$ first used in a traditional liquid DSSC, but this cell failed due to the dissolution of the perovskite in the electrolyte[15]. Soon, they were also employed in ssDSSC, but these devices keep employing spiro-OMeTAD as the HTM[16]. However, it was discovered that the perovskite could also act as the HTM itself. Nevertheless, a HTM is still in use by most current devices.

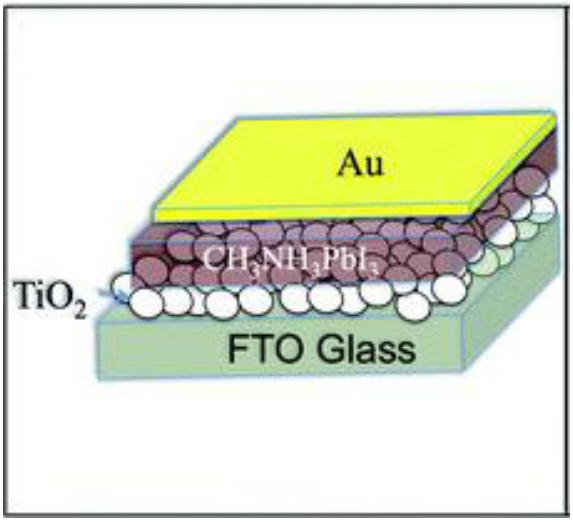

Figure 2.6

Schematized energy diagram of a DSSC[17]

The structure of a perovskite ssDSSC is shown in **Figure 2.6**[17]. Above a substrate of conducting glass, a compact layer of TiO_2 is deposited. Above it lays the perovskite layer, acting as the light absorber. The perovskite, in turn is covered by the HTM, typically the spiro-OMeTAD. A metallic layer at the top

finally acts as the counterelectoder, closing the circuit. A smooth and homogeneous covering is required, free of pinholes, since if unwanted contacts were to exist between the non-consecutive layers (such as a contact between the TiO_2 and the HTM, or the perovskite and the countereectrode), no photovoltaic effect will occur. There is, however, still some debate regarding the best deposition technique to achieve it. The most commonly used perovskite is the $CH_3NH_3PbI_3$, but similar compounds with either bromide or chloride had been tried as well[18]. Perovskites with formamidinium as the organic part or Cs as the metallic cation were also tried, but they were proven to have less efficiencies that the $MAPbI_3$ compound.

The research regarding perovskite ssDSSC has seen a dramatic increase, tied with the increase in performance of the cells. Both effects are shown in **Figure 2.7**, which shows the number of publications about perovskite solar cells as of 2/1/2015[19]. The perovskite solar cells are an exciting topic in today's material science research and will continue to be so in

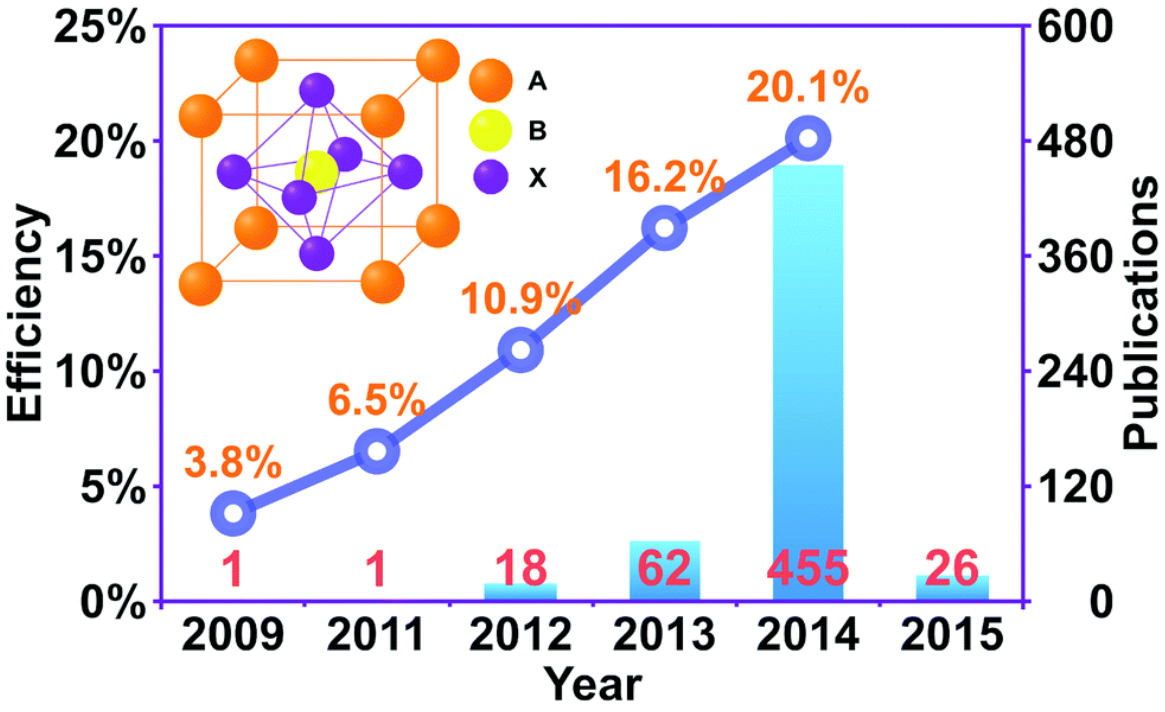

Figure 2.7

Growth of both research and efficiency of perovskite solar cells[19]

the foreseeable future.

2.3 Perovskite crystal structure[20]

It is doubtful that when Gustav Rose discovered the calcium titanate ($CaTiO_3$) in Russia and decided to name it after the Russian mineralogist L. A. Perovski he could imagine the importance of his discovery for the future of solar cells[18]. Regardless of that, it was soon realized that many other compound shared the same peculiar crystal structure of the new mineral, so they began to be called by the same name. This way, compounds with perovskite structure have a generic formula of ABX_3, where A and B are cations of very different sizes, the A cation being larger, and X is an anion.

The ideal perovskite structure of a compound ABX_3 has a cubic unit cell, where each A cation is surrounded by 12 X anions inside a cubooctahedral, and each B cation is surrounded by 6 X anions forming BX_6 octahedra. Meanwhile, the BX_6 octahedra themselves form a three dimensional structure in which every octahedron shares all of its vertexes with neighboring octahedra. In the cavity created by eight of those octahedra is located the A cations, balancing the whole structure. This structure can be seen in **Figure 2.8**.

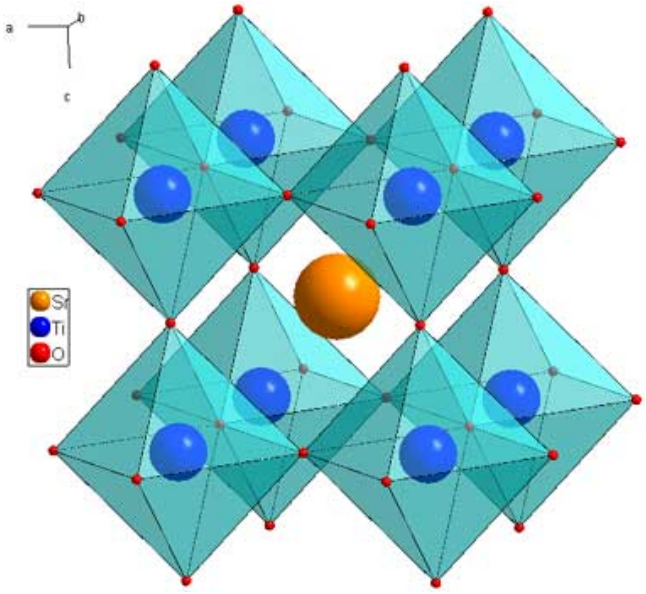

Figure 2.8
Structure of a perovskite

The ideal cubic perovskite structure is only reached when the ionic radii of A,B and X ions fulfill a particular criterion. If the ionic radii are out of the ideal ratio, the compound displays a distorted perovskite crystal structure with a cooperative tilting and rotation of the BX_6 octahedra. Its crystal symmetry also becomes lower than the ideal cubic cell. To predict this effect,

a tolerance factor, *t*, was proposed by Goldschmidt in the early 1920. It follows the following formula[21]:

$$t = \frac{r_A + r_X}{\sqrt{2}(r_B + r_X)}$$

Where r_A, r_B and r_X are the ionic radii of the cations A and B, and the anion X. For an ideal cubic structure *t* should be equal to 1. However, since the Goldschmidt factor deals with ionic radii, it should be remembered that it is just a semi-empirical formula. In reality, structures with *t* within 0.9 and 1.0 remain their cubic structure. This range is broadened when the distorted structures are also taken into account[22].

The most commonly used perovskite for photovoltaic applications, the $MAPbI_3$, is a somewhat peculiar example in that the Pb^{2+} cation takes the B position, while it commonly occupies the A position. This unusual location is only possible because a large electropositive cation, $(CH_3NH_3)^+$, occupies the A position[23].

3 OBJECTIVES

The main objective of this dissertation is the synthesis and characterization of hybrid organic-inorganic perovskites for its possible use in solid-state dye sensitized solar cells. The focus will be on the hybrid perovskites $(CH_3)_2NH_2PbI_3$ and $CH_3NH_3PbI_3$, and their capabilities as light absorbers. Furthermore, the particle size of the colloids of the precursor solutions will be studied, as well as its relationship with the thin film morphologies and the influence of various additives.

To that end, the following steps will be taken:

- Synthesis of the precursor compounds: $(CH_3)_2NH_2I$ (DMAI) and CH_3NH_3I (MAI)
- Measurement of the particle size of the colloids in the precursor solutions.
- Deposition of thin films in glass substrates using the one-step spin-coating and the two-step spin-coating techniques.
- Study of the optical properties of the $DMAPbI_3$ compound.
- Characterization of all the obtained thin films using XR powder diffraction and the Scanning Electron Microscopy (SEM).
- Study of the effect of the MACl as an additive on the $MAPbI_3$ precursor solutions, both in particle size and thin film morphology.
- Study of the effect of various additives on the $DMAPbI_3$ precursor solutions both in particle size and thin film morphology.

4 EXPERIMENTAL PROCEDURE

4.1 Synthesis of the precursors

Before any work could be done on the deposition of the thin films themselves, the precursors had to be synthetized, since neither the methyamonnium iodide (CH_3NH_3I) nor the dimethylammonium iodide ($(CH3)_2NH_2I$) were commercially available. The method employed for the synthesis was described in the bibliography[24], if somewhat sparingly.

4.1.1 $(CH_3)_2NH_2I$

12 mL of dimethylamide 40% (wg.) in water (0.0949 mol) were dissolved in 50 mL of ethanol in a round-bottom flask. 5 mL of hydriodic acid 47% (wg.) in water (0.0275 mol) were added while under magnetic stirring in an ice and water bath. After letting the mixture react for an hour the solvent was eliminated in the rotary evaporator. An orange precipitate was formed on the walls of the flask. That precipitate was redissolved in 10 mL of heated ethanol and transferred to a crystallizer. The mixture was left for a day to recrystallize, even though some white crystals had already began to form when the ethanol cooled. The next day, the product dimethylammonium iodide (DMAI) was recovered by vacuum filtration and washed with small quantities of cold ethanol.

It should be noted that, even though the bibliography indicates the washing with diethyl ether, when that was attempted the DMAI was immediately dissolved and washed to the Erlenmeyer flask. The ether had to be eliminated in the rotary evaporator and the product recrystallized once again. It was recovered by vacuum filtration and washed with cold ethanol, as already mentioned.

The DMAI was in the form of a white powder, which was sent to XRPD for analysis. A total of 1.644g of product was obtained, achieving a yield of 34.5%. This quantity was enough for all the made thin films, and there was no need to repeat the synthesis.

4.1.2 CH_3NH_3I

A similar method to the one used in the synthesis of DMAI was used for the methylammonium iodide (MAI), only with bigger quantities of both reagents and solvent. 24 mL of methylamide 33% (wg.) in ethanol were mixed with 10 mL of hydriodic acid (same as before) in 100 mL. The reaction time was also longer, at 2 hours, after which the solvent was eliminated in the rotary evaporator. This time the product recovered by the vacuum evaporation was washed directly with cold ethanol.

The product was also in the form of a white powder, which was sent to XR powder diffraction (XRPD) for analysis. Since the MAI was more commonly used than the DMAI, the synthesis of the former had to be repeated several times.

4.1.3 Synthesis of the bulk perovskite

The synthesis of the perovskite was attempted using a mortar. To that end 75 mg of DMAI ($4.33 \cdot 10^{-4}$ mol) were mixed with 200 mg of commercially available PbI_2 ($4.33 \cdot 10^{-4}$ mol) in a mortar to obtain $DMAPbI_3$, which still had a white color.

The $MAPbI_3$ was also synthesized in a mortar, mixing stoichiometric quantities of MAI and PbI_2. In this case there was a dramatic change of color: from the yellow of the PbI_2 and the white from the MAI (**Figure 4.1**) to a pitch black due to the perovskite (**Figure 4.2**).

Figure 4.2
MAI and PbI_2 before mixing

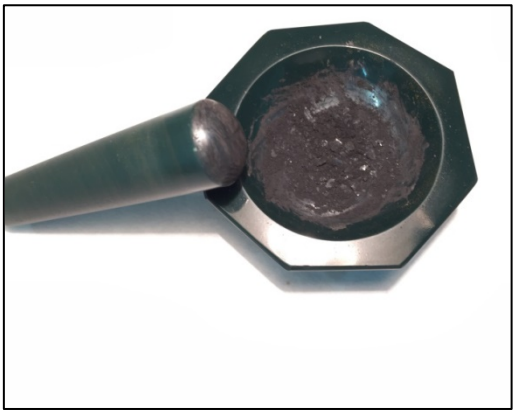

Figure 4.1
Obtained perovskite after mixing

4.2 Preparation of the substrate

The substrates employed at the beginning were originally glass specimen holders for an optical microscope, manually cut to the required size (approx. 3x3 cm). To avoid the interference of dust in the deposition of the films the substrates were thoroughly washed with distilled water with soap and then rinsed with more distilled water.

Halfway during the experimental procedure new glass substrates with a layer of a conductive material were obtained. These could better simulate the morphology of a proper solar cell and were used from that point onwards. The thin films were only deposited on the conductive layer.

4.3 Deposition methods

Two methods were employed for the deposition of the thin films: the one-step deposition and the two-step deposition. These were found in the bibliography[25] and were reproduced in the laboratory.

4.3.1 One-step deposition

In the one-step spin-coating technique, a precursor solution of the desired product is prepared. This solution is spread over the substrate with the help of a spin-coater. The substrate is then heated, so all the solvent evaporates, leaving just a thin film of the perovskite.

In the one-step procedure, a precursor solution of both PbI_2 and MAI (or DMAI) is prepared beforehand. To that end 0.395 g of MAI and 1,157 g of PbI_2 are dissolved in 2 mL of dimethylformamide (DMF), to obtain a solution with a 1.25 M concentration of $MAPbI_3$. When preparing the precursor solution of DMAI, instead of MAI, 0.363 g of DMAI was dissolved with the same amount of PbI_2. Since the PbI_2 proved difficult to dissolve, the solutions are left heating (at around 60° C) under magnetic stirring overnight. Finally, a yellow solution of $MAPbI_3$ is obtained. The $DMAPbI_3$ has a more orange color.

The substrate is attached to the moving part of the spin-coater with the help of some blue-tack, as shown on **Figure 4.3**. Then, the precursor solution is placed on top of the substrate with a micropipette, and spread until it covers all the substrate, like in **Figure 4.4**. Initially the volumes of the precursor solution were as low as 20 µL were used, but it was soon proved that they were unable to completely cover the substrates. The amounts were progressively increased to 150 µL. Once the substrate is covered with the solution, the spin-coater is started, with the following parameters:

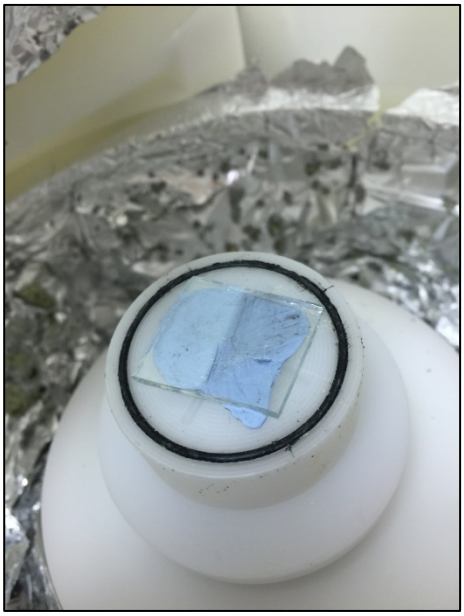

Figure 4.3

Attaching the substrate

- Acceleration: 500 rpm/s
- Maximum speed: 3000 rpm
- Total run time: 20 s

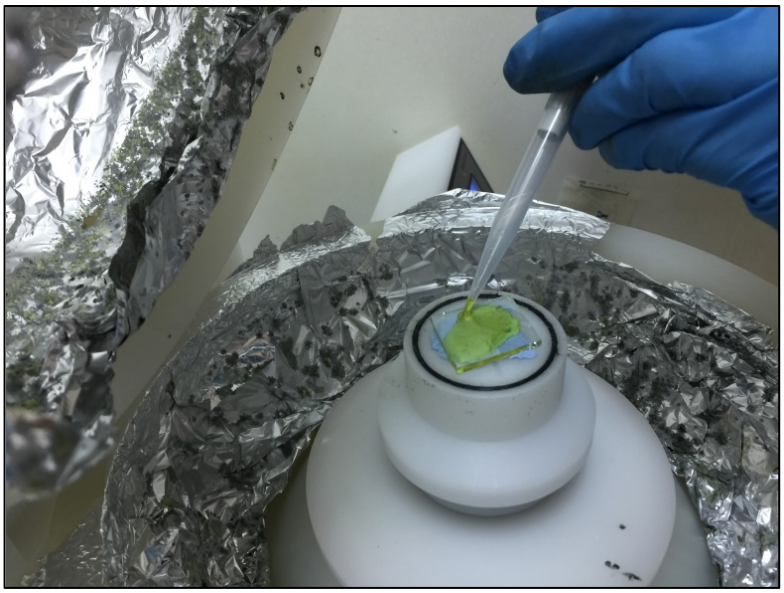

Figure 4.4

Spreading the precursor solution

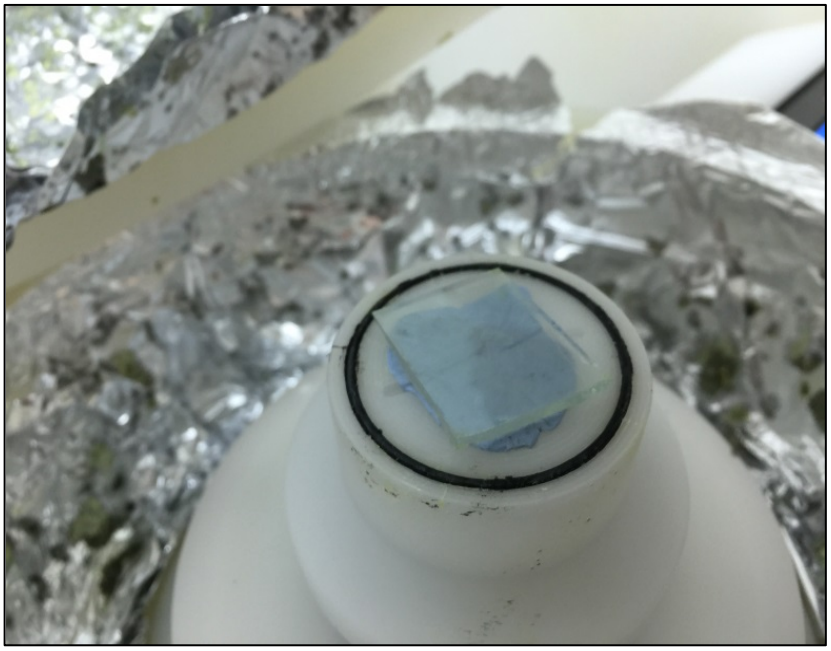

Figure 4.6

Substrate after the spin-coating

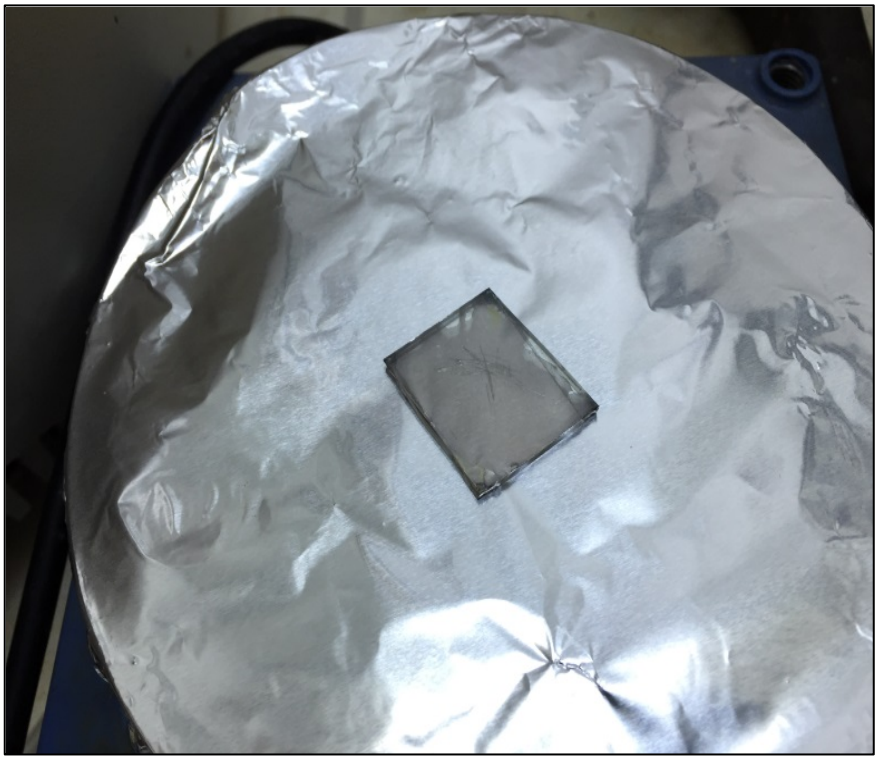

Figure 4.5

Substrate on the hot plate

Those parameters were left unchanged in all experiments, unless otherwise noted. After the spin-coater had stopped, it would seem like there was no solution left in the substrate, as shown on **Figure 4.5**. However, once the substrate was placed on a hot plate a black color will soon star to show, as in **Figure 4.6**. The substrate was left on the hot plate for about 5 minutes, at a temperature of approximately 70° C. Afterwards it was transferred to an oven at 100-150° C and was left heating for another five minutes. After recovering the substrate the black color had intensified, as can be seen in **Figure 4.7**.

The one-step deposition technique was the most used technique throughout the whole procedure, and the obtained films were used to measure the optical properties.

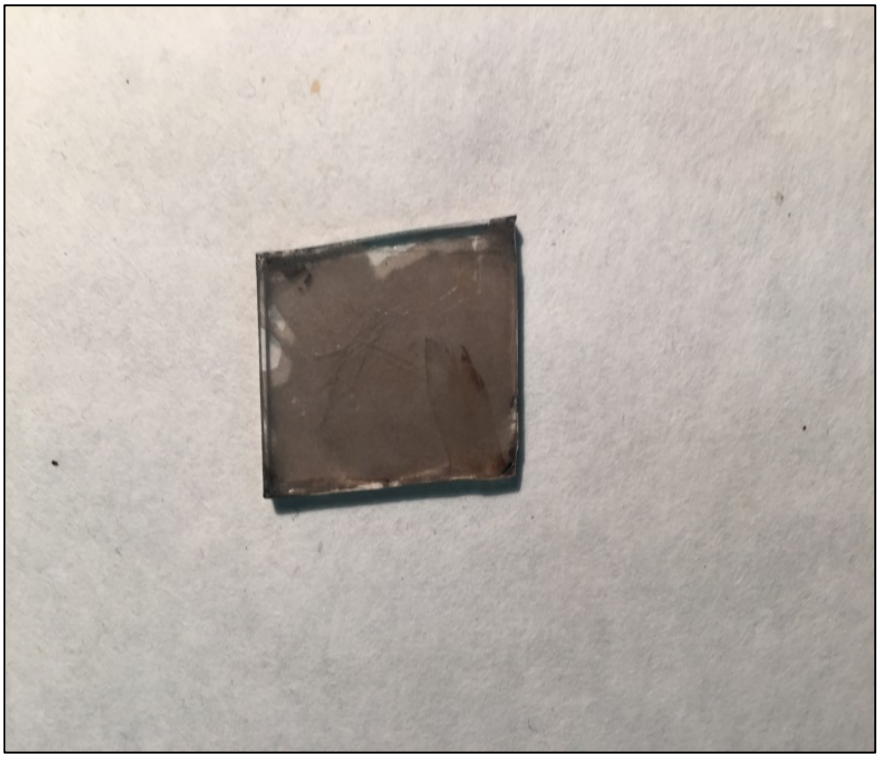

Figure 4.7

Substrate after the heating treatment

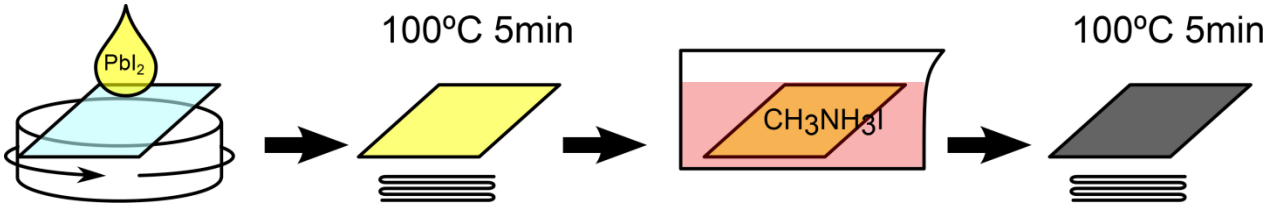

Figure 4.8

Two-step technique diagram

4.3.2 Two-step deposition

The two-step deposition technique is a variation of the one-step technique. In this version the two reagents needed for the synthesis of the perovskite, PbI_2 and DMAI, are deposited separately on the substrate. First, the substrate is covered by spin-coating a solution of PbI_2 and then the solvent is evaporated in the oven. The resulting film thin is submerged in a solution of DMAI and the solvent evaporated again in the oven. The technique is resumed in the **Figure 4.8**.

The precursor solution of PbI_2 was prepared dissolving 0.9231 g of PbI_2 in 2 mL of DMF, to achieve a concentration of 1 M. The PbI_2, however, proved extremely difficult to dissolve in DMF, needing long times of heating and magnetic stirring. Furthermore, after the heat and the stirring were removed, the PbI_2 tended to precipitate again. Despite these difficulties, a solution stable enough to be spin-coated was obtained. The parameters used in the first deposition were identical to those of the one-step technique (Acceleration: 500 rpm/s; speed: 3000 rpm; time: 20 s). The solvent was evaporated in the hot plate for 4 minutes and then in the oven for another five minutes, at 100° C. A yellow thin film of PbI_2 was observed to be formed.

A second solution was prepared, dissolving 40 mg of DMAI in 2-propanol, to achieve a concentration of 0.063 M. The substrate previously covered with the thin film of PbI_2 was submerged in this new solution for a minute. Then, it was heated again in the oven at 100° C. The yellow film, however, barely changed its color.

The two-step technique was barely used. After the first try with DMAI it was abandoned in favor of the one-step technique. This was due to the difficulties in obtaining a proper pre-

cursor solution of PbI_2 and later XR-diffraction patterns showed little perovskite formation and a large excess of PbI_2 in the obtained thin films. Our efforts were redirected towards the optimization of the one-step deposition.

4.4 Additives

Besides the different deposition methods employed, the influence of the composition of the precursor solution was also studied. The main objective was to achieve a good morphology of the thin films since, as it will be shown, a homogenous thin film was not deposited.

4.4.1 MACl as an additive

An attempt to change the morphology of the deposited film was made by adding different amount of chloride to the precursor solution of $MAPbI_3$. It had not been proved that the chloride could substitute the iodide in the perovskite structure, but it could affect the deposition mechanism, as was later proven by the bibliography[26]. The $MAPbI_3$ precursor solution was chosen to better reproduce the procedure of the bibliography and because the deposition was better optimized than in the $DMAPbI_3$.

To examine the effects of the chloride on the morphology, a systematic approach was employed, reproducing that of the bibliography[26]. Four solutions were prepared, in which the stoichiometric ratio of the MAI and the PbI_2 was kept constant at 1:1. To each solution, however, increasing amounts of MACl were added, at molar ratios of 0.5; 1; 1.5 and 2. The concentration of PbI_2 was kept at 0.628 M in a volume of 4 mL of DMF. These solutions were then deposited on the substrates using the one-step spin-coating and the dip-coating techniques. Also, the particle size of the solutions was measured.

4.4.2 DMAX as additives

A final experiment was attempted in which several MAX and DMAX compounds (methyl or dimethyl ammonium halides, where X is either Cl or I) were used as additives to obtain a better deposition of the $DMAPbI_3$ compound, as well as o reduce the particle size of the

precursor solutions. To that end, the following solutions were made (always in 2mL of DMF):

- A MAI/DMACl/PbI_2 solution at a molar ratio of 1:1.5:1
  - 0.395 g of MAI
  - 0.305 g of DMACl
  - 1.157 g of PbI_2
- A MACl/DMAI/PbI_2 solution at a molar ratio of 1:1.5:1
  - 0.166 g of MACl
  - 0.648 g of DMAI
  - 1.157 g of PbI_2
- A DMAI/DMACl/PbI_2 solution at a molar ratio of 1:1.5:1
  - 0.432 g of DMAI
  - 0.305 g of DMACl
  - 1.157 g of PbI_2

The particle size of the solutions was then measured and the solutions themselves were deposited by the one-step spin coating technique.

Figure 5.1

XR-diffractometer

5 INSTRUMENTATION

Throughout the experiments several techniques were used to identify the obtained products and to analyze the morphology of the resulting thin films. Furthermore, several more techniques were used to gain an insight in the properties of the perovskite, as well as the different solutions employed. The most employed techniques were, in no particular order: X-ray powder diffraction (XRPD), UV-Vis spectroscopy for solid samples, scanning electron microscopy (SEM) and particle size measurement.

5.1 X-ray powder diffraction (XRPD)[27]

Due to the small time of analysis and sample size, as well as the fact that both bulk and deposited samples could be analyzed, the XRPD technique was used for the characterization of all samples. Since XR diffraction patterns were obtained for both the reagents and the products, the different impurities could also be identified. The instrument used was the diffractometer D5000 SIEMENS from the SAI (Servicios de Apoio a Investigación), shown in **Figure 5.1**[28].

The theoretical basis for the XR-diffraction is explained by the Bragg's law, which is schematized in **Figure 5.2**. The diffraction is considered as simultaneous reflections of the X-ray beams by various lattice planes belonging to the same family (or more appropriately, by the atoms lying in those planes). In the figure, θ is the angle between the prima-

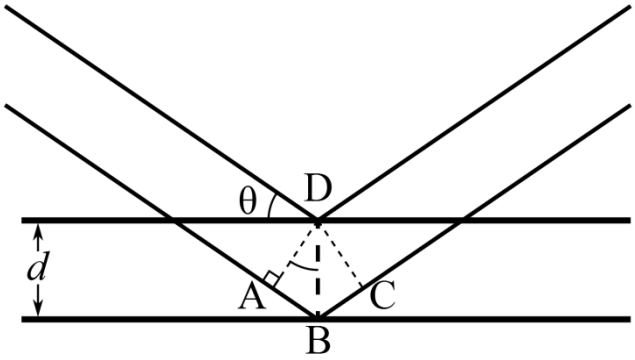

Figure 5.2

Bragg's law diagram

ry beam and the planes. The difference in the length of the path of the beams scattered at points B versus those scattered at D equals:

$$\overline{AB} + \overline{BC} = 2d\,sin\,\theta$$

If that magnitude is a multiple of the wavelength of the X-rays beams, λ, then the beams will be in phase, leading to maximum positive interference. Otherwise, the beams will cancel each other through destructive interference.

A XR-diffractometer is able to launch an X-ray beam at different angles at the sample, and then detect the scattered rays. The intensity of the rays is usually represented versus *2*θ. The corresponding peaks depend on the position of the crystal planes, and are unique for each structure. It is possible, using advanced techniques, to determine the actual structure of the compound from the scattering data, but that remains outside the scope of this dissertation.

5.2 Scanning electron microscopy (SEM)

The scanning electron microscopy was a key technique in analyzing the morphology of the thin films and thus determining whether a proper homogeneous film had been obtained. Consequently almost all films were observed in the SEM. The instrument employed was a benchtop SEM, model JMC-5000 NeoScope, shown in **Figure 5.3**[29].

Figure 5.3

Employed SEM

5.2.1 Fundaments[30]

The scanning electron microscopy is based in the interaction of an electron beam with the surface of the sample. These interactions can be classified in elastic collisions, in which only the trajectory of the colliding elec-

tron is changed, and inelastic collisions, in which part of the energy of the electron is transferred to the solid. The electrons suffer numerous collisions as they advance through the sample, constantly changing directions, which eventually causes most of them of leave the sample as back-scattered electrons (BSE). The resulting beam of back-scattered electrons has a wider angle than the original beam.

Some of the electrons, however, can lose some energy through inelastic collisions. That energy is transferred to the sample, and can cause electrons with energy less than 50 eV to be emitted from the sample itself, together with some X-ray radiation. The emitted electrons are called secondary electrons, and the resulting beam is no much wider than the original beam. For this reason, the secondary electrons are the most commonly used in the SEM technique; though the back-scattered electrons can also be analyzed, as well as the resulting X-rays[30]. Those X-rays have a unique energy for each element, and their analysis can give qualitative and quantitative information in the sample, using the Energy-dispersive X-ray spectroscopy (EDX) technique.

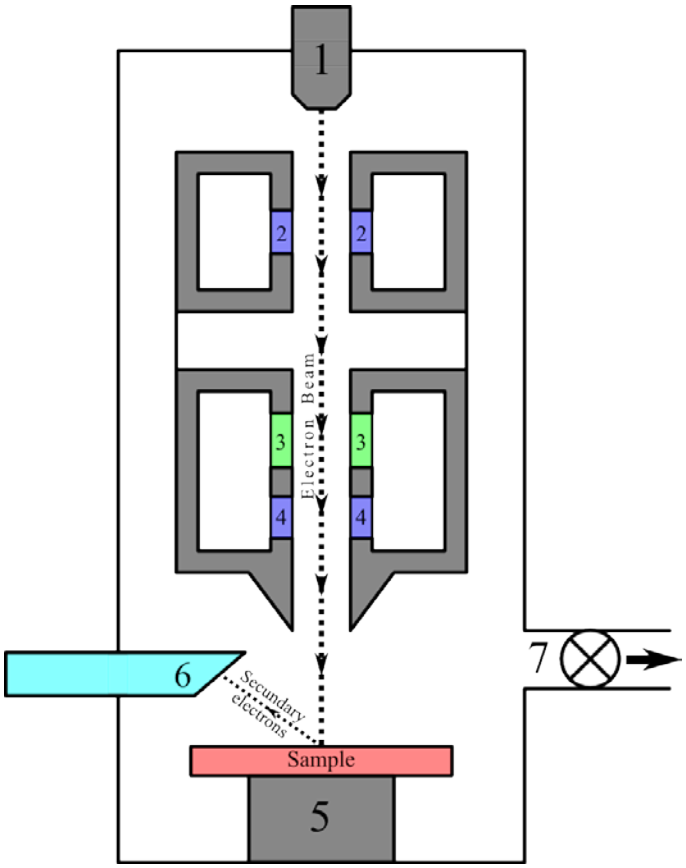

Figure 5.4

Parts of a Scanning Electron Microscopy

5.2.2 Instrument[31]

The parts of an SEM are summarized in **Figure 5.4**, and are as follows:

1. Electron gun: It creates the electron beam. The electrons themselves are generated in a filament (such a heated tungsten wire, though other materials can be used) and then they are accelerated by the voltage between the filament (cathode) and

an anode.

2. Condenser lens: They are a set of magnetic lens that focus and regulates the electron beam coming from the electron gun.
3. Scanning coils: Also known as deflector plates, they change the direction of the electron beam in the *x* and *y* axis, allowing it to scan a rectangular area of the sample surface.
4. Objective lens: As the last set of lens before the sample they bring the electron beam into focus.
5. Specimen holder: It keeps the sample in place and allows it to be moved in the *x* and *y* directions (in the sample plane) as well as in the *z* direction (specimen height).
6. Secondary electron detector (SED: It collects the secondary electrons coming from the sample to give a topographical image. Since the secondary electrons usually have low energy, a positive bias is applied to a cage in front of the detector, which directs the electrons into the detector itself.
7. Vacuum pump: To reduce the scattering of the electron beam before reaching the sample is necessary to work in a vacuum. To that end, a vacuum pump is fitted to the system.

5.3 Particle size measurement[30]

The most common technique for measuring the particle size of a sample is the dynamic light scattering technique (DLS). This technique is based in the Doppler widening of the Rayleigh dispersed light as a result of Brownian motion. In macromolecular solutions, the width of the Reyleigth line correlates to the diffusion coefficient, D_T. For a spherical particle D_T is also related to the hydrodynamic diameter, d_H, following the Stokes-Einstein relationship. It should be noted that many other factors, such as the temperature of the sample and its viscosity also take part in the measurement, so they must be known and controlled.

The parts of a DLS instrument are shown in the **Figure 5.5**, and are as follows:

1. Laser: In the used instrument, this was a red diode laser of a nominal wavelength of 640 nm. It provides the source of light that is scattered by the sample.

2. Lenses: They focus first the light coming from the laser into the sample, and then the dispersed light into the detector.
3. Sample cell: They are either plastic or quartz cells, square or cylindrical. They can hold up to 4 mL of sample.
4. Detector: A photomultiplier tube that converts the light signal coming from the sample into an electric signal.
5. Signal processing: Processes the electric signal into the data that is displayed in the computer.

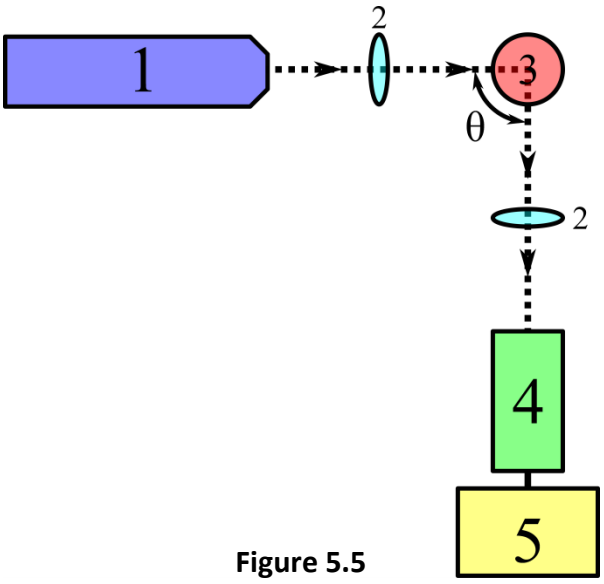

Figure 5.5

Parts of a DLS instrument

The letter θ represents the scattering angle at which the scattered light is measured. In most cases, as well as in the used instrument, it equals 90°.

The instrument at our disposal was a 90Plus/BI-MAS, Multi Angle Particle Sizing Option, from Brookhaven Instruments Corporation. For the measurements to be reproducible, they had to be put in an ultrasonic bath for five minutes. After approximately one minute for stabilization the samples were put in cylindrical quartz cells (the plastic cells provided by the manufacturer could not be use since our solvent, THF, attacked the plastic) and introduced in the apparatus.

5.4 UV-Visible

To measure the optical properties the V650 UV-Vis Spectophotomer was employed. The measuring of the solid samples, such as the thin films was possible using a 60 mm integrating sphere. The software provided with the equipment also made possible the calculation of the band gap of the compounds. This was employed using the Tauc plot, which represents

the $\alpha h\nu^{1/r}$ value, where α is the absorption coefficient and r depends on the nature of the transition, against the $h\nu$ value. The lineal range of the plot is where absorption takes place and extrapolating to the x-axis allows the value of the band gap to be calculated.

6 RESULTS AND DISCUSSION

The following section will be focused in the properties of the synthetized $DMAPbI_3$ in relation to its application in solar cells. The use of additives to achieve good thin film morphology, especially in changing the particle size of the precursor solutions will be studied as well.

6.1 Properties of the $DMAPbI_3$

As it was mentioned before, the literature concerning the $DMAPbI_3$ was somewhat lacking. Therefore, much of the groundwork had to be done either by ourselves or by our laboratory companions.

A crucial step was determining the structure of the compound. It was speculated that it would have a perovskite structure similar to the $MAPbI_3$, but as it was later proved, this was only partially true. A single crystal of $DMAPbI_3$ was successfully synthetized by dissolving it in THF, and then slowly evaporating the solvent. The resulting crystal was analyzed by the X-ray single crystal diffraction technique, and the obtained data was used to predict the structure of the compound. This was not done by us, but our laboratory partners, who then provided us with the crystal structure of $DMAPbI_3$

6.1.1 Crystal structure and XRPD

The obtained structure can be seen in **Figure 6.1**. As it can be observed, it is not a proper perovskite (compare with **Figure 2.8**): The BX_6 octahedra do not share just one vertex with the neighboring octahedra, but a whole face. Furthermore, they only share it with the octahedra directly above and below (*c* direction), but no with those on the sides (*a* and *b* directions). This distortion of the perovskite structure is due to a larger tolerance factor, *t*, caused by the bigger size of the DMA ion in comparison with the MA ion. The structure loses symmetry as the octahedra are less connected.

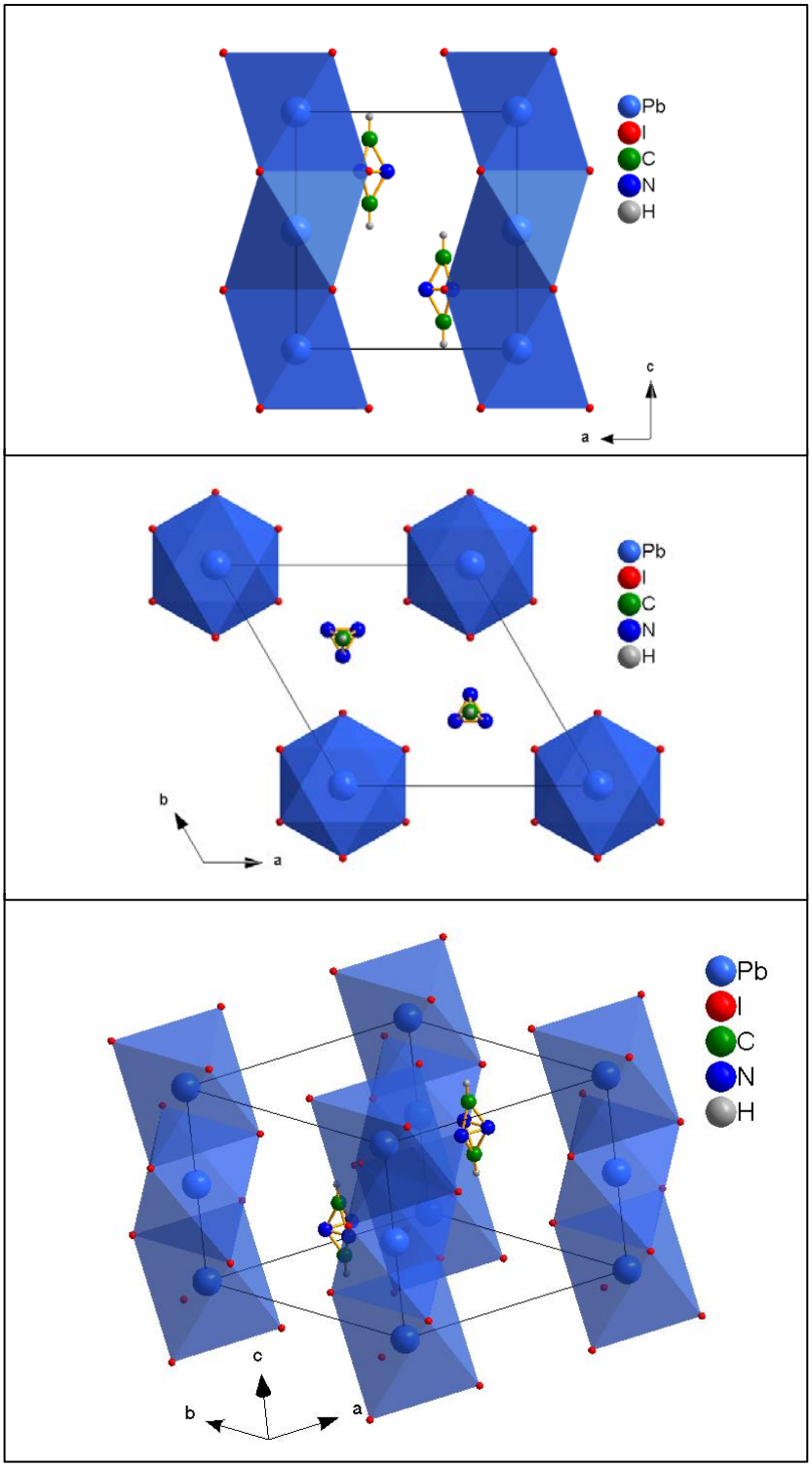

Figure 6.1

Different views of the structure of $DMAPbI_3$

Furthermore, the cubic unit cell is lost and substituted by a hexagonal one, making the compound to be known as a hexagonal perovskite.

The XR-diffraction pattern was obtained for the bulk synthetized $DMAPbI_3$, as indicated before, and compared with the theoretical pattern for the crystal structure of the single crystal, as shown in **Figure 6.2**. As can clearly be seen, the two patterns are very similar, showing that the perovskite was successfully synthetized almost without impurities.

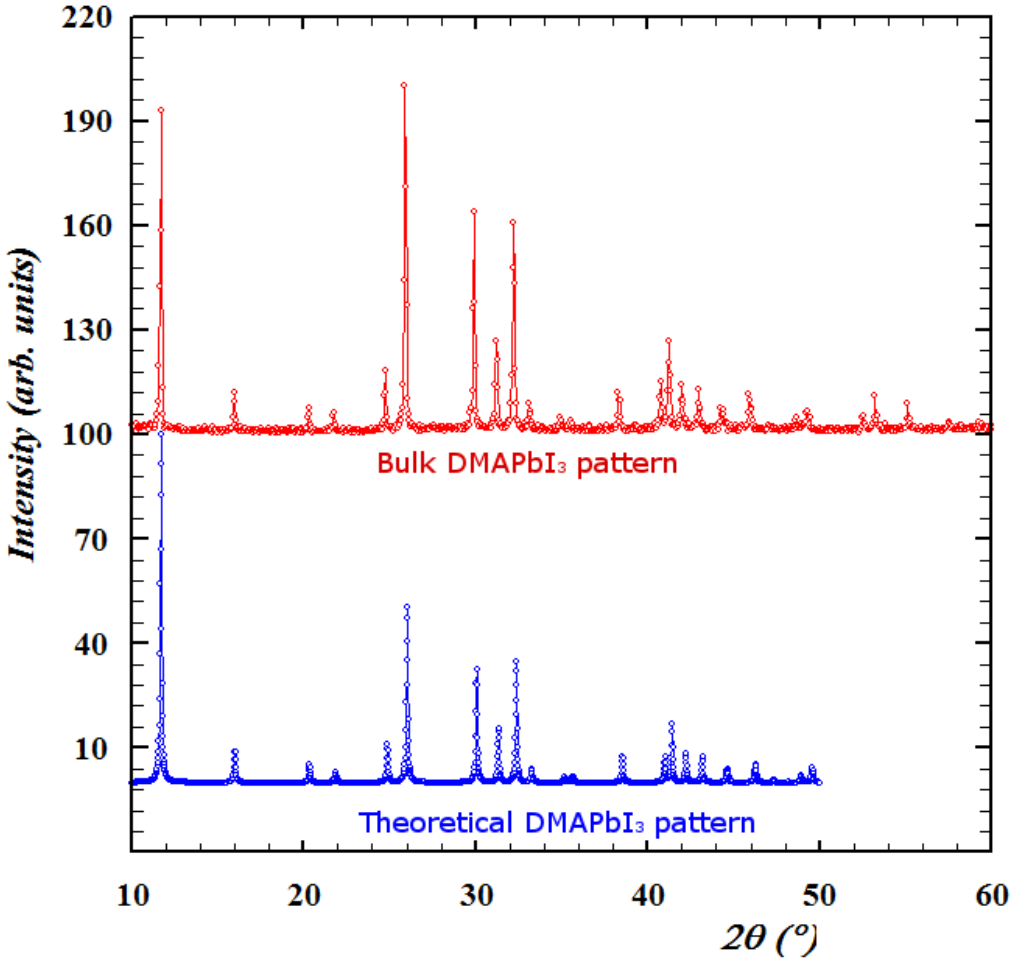

Figure 6.2

The XR-diffraction pattern of DMAPbI3

6.1.2 Optical properties

Using a 60 mm integrating sphere, the UV-Vis spectra of the $DMAPbI_3$ was obtained, and it is shown in **Figure 6.3**, superimposed with the range of the visible spectrum and the spectra from the $MAPbI_3$. For a material to be a good photovoltaic material it is necessary that it absorbs in the region of the visible spectrum and the near infrared (λ>700 nm). Unfortunately, as it can clearly be seen, the $DMAPbI_3$ does not absorb in those wavelengths, which also explains the lack of color in the prepared films. The only relevant absorption of the material takes place in the ultraviolet region, where little radiation comes from the sun. Furthermore, the electronic band gap of the compound was calculated based on the above data to be 2.81 eV, using a Tauc plot. This further limits the uses of the $DMAPbI_3$ as a photovoltaic material. The band gap is too high to be a proper semiconductor and is also too high to be overcome by the absorbed photons.

In contrast, the $MAPbI_3$ is capable of absorbing both in the visible spectrum and in the near

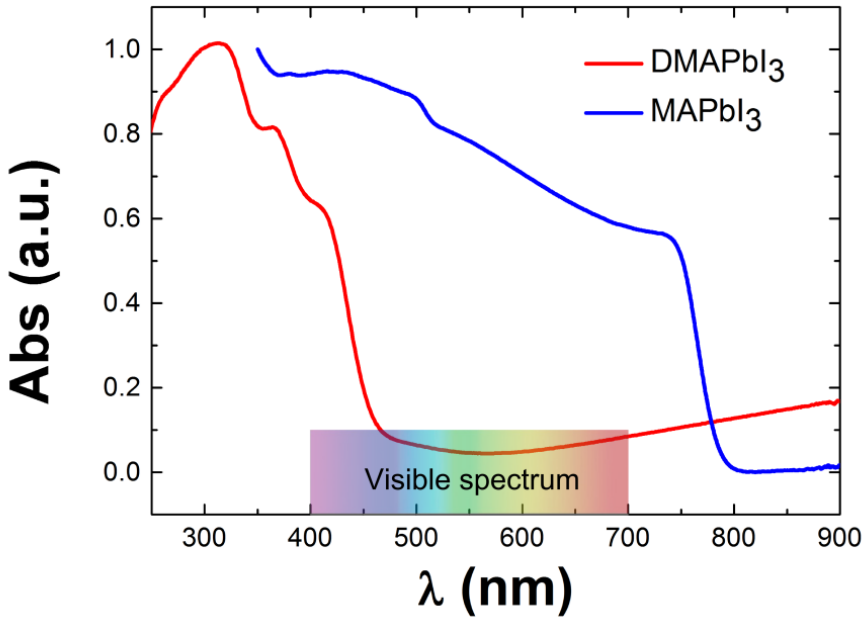

Figure 6.3

The absortion spectrum of the $DMAPbI_3$

infrared, as is also shown in the graph. Also, its bandgap is a more appropriate 1.57 eV, according to the data we obtained using the same procedure as for the $DMAPbI_3$.

However, the band gap of 2.81 eV and the absorption near the ultraviolet spectrum raises the possibility of using the $DMAPbI_3$ as the basis of a blue LED. This could lead an important revolution in terms cheap light sources with high efficiencies.

6.2 $DMAPbI_3$ thin films

As was previously described (page 25), several thin films of $DMAPbI_3$ were prepared using either the one or the two-step spin-coating deposition technique. Furthermore, three films were prepared using a mixture of DMAI, MAI, MACl and DMACl; together with PbI_3. The resulting films were analyzed by XRPR and observed under the SEM.

6.2.1 One-step technique

Using the 1-step spin-coating technique a thin film of $DMAPbI_3$ was successfully deposited. It should be noted, however, that while in the case of the $MAPbI_3$ thin films a dramatic change of color was observed after the thermal treatment, there was no such change in the case of the $DMAPbI_3$. This lead to some doubts regarding the success of the deposition, but a closer look to the resulting XR-diffraction patterns proved otherwise.

The obtained pattern is shown in **Figure 6.4**, superimposed with the theoretical pattern shown before. As it can be seen, there is a very good correlation, proving that the $DMAPbI_3$ was indeed formed. The only exception is the peak at $2\theta = 12.7°$, shown with more detail in **Figure 6.5**, which is due to leftover impurities of PbI_2.

It can also be observed that no all peaks from the theoretical pattern are present in the empirical one. This indicates that growth only occurs in some directions, while in others there is almost no growth.

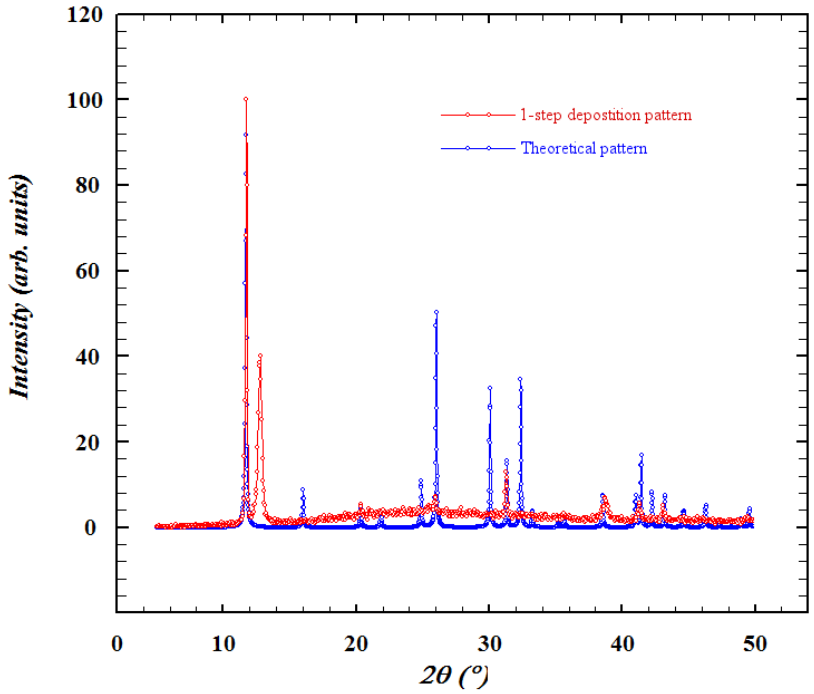

Figure 6.5

The XR-diffraction pattern of a thin film of DMAPbI3

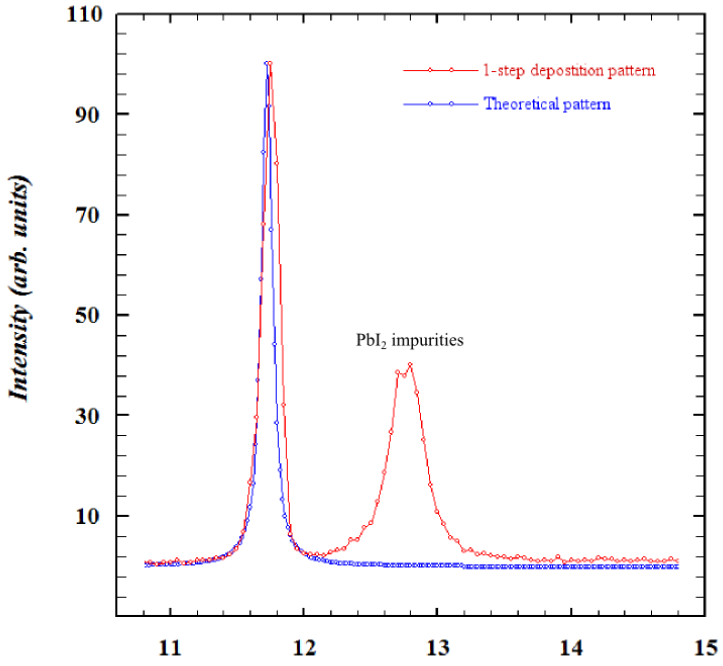

Figure 6.4

Detail of the XR-diffraction pattern of a thin film of $DMAPbI_3$

This is further corroborated by the images obtained by the SEM. As shown in **Figure 6.6**, the $DMAPbI_3$ does not form a homogeneous layer, but instead grows in the form of small needle-like structures. When the thin film of $MAPbI_3$ was synthetized the same needle-like structures were observed, although the tended to be bigger and better formed. This morphology was believed to be due to a high particle size of the precursor solutions, which seemed to be confirmed when the particle size could not be measured due to being outside the range of the instrument.

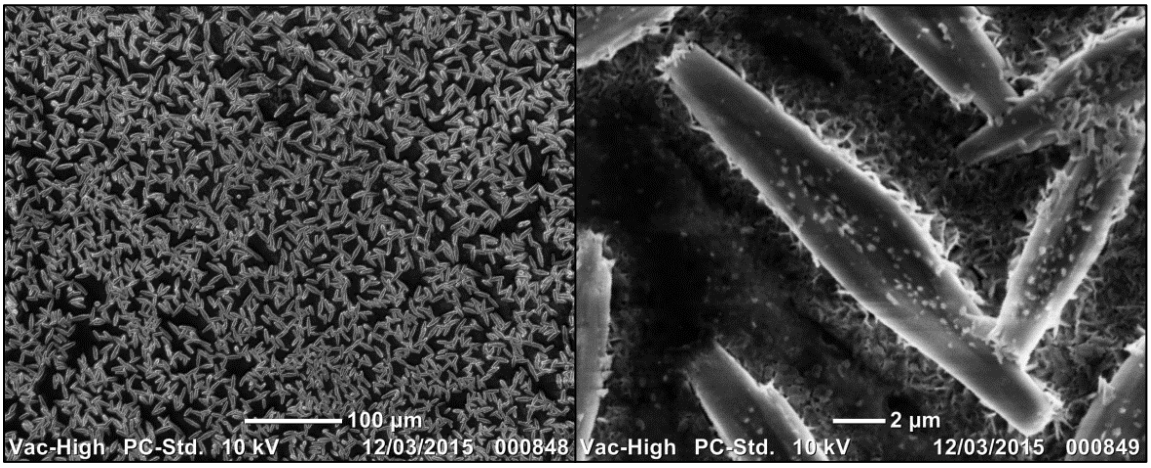

Figure 6.6

Morphology of the $DMAPbI_3$ thin film

6.2.2 Two step technique

The deposition of another thin film of $DMAPbI_3$ layer was also attempted using the two-step technique. However, this was not successful, as was observed during the experiment, since no thin film seemed to be deposited. Regardless, the sample was analyzed by XRPR; and the resulting pattern is shown in **Figure 6.7**, once again superimposed with the theoretical pattern. In the inset in the figure it can be seen that, although some $DMAPbI_3$ was formed, there were large quantities of PbI_2 left. Furthermore, the low signal/noise relationship indi cates that almost no product was left in the substrate. For these reasons, this film was not observed under the SEM.

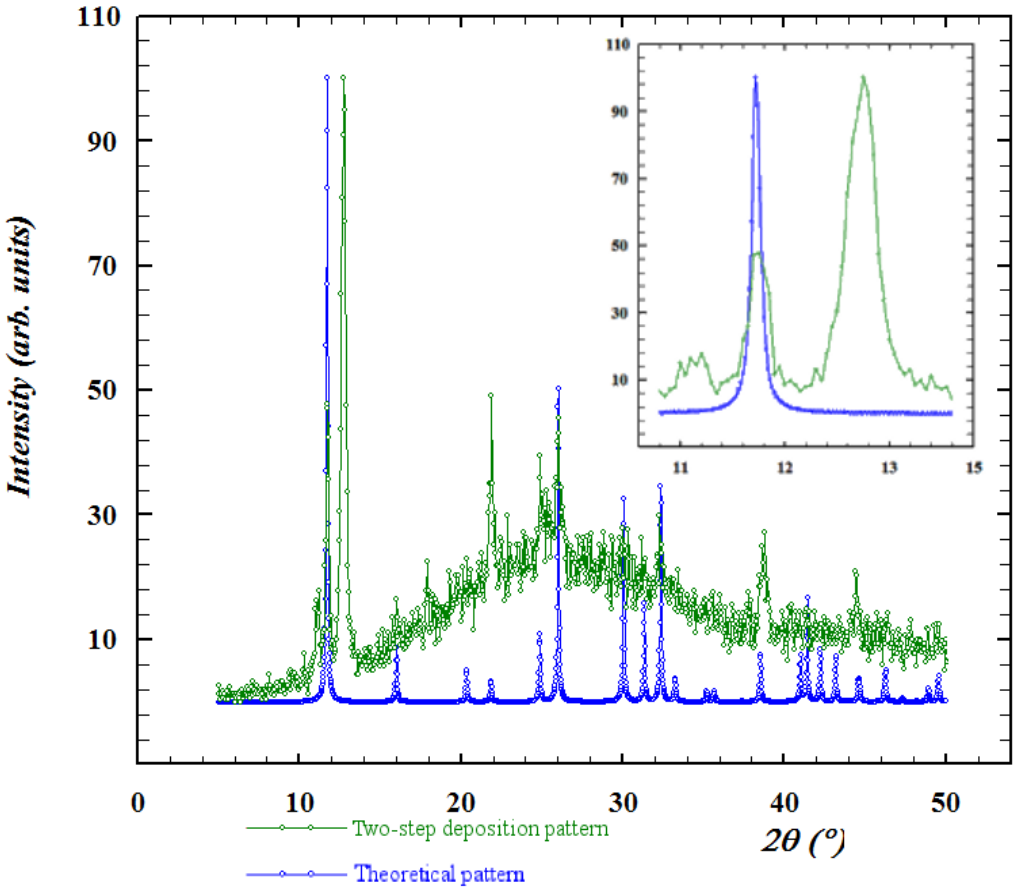

Figure 6.7

The XR-diffraction pattern of DMAPbI3

6.3 MACl as an additive in $MAPbI_3$ precursor solutions

The failure to deposit thin films with a proper morphology led to the study of the influence of additives in achieve the right morphology. This was first attempted with the $MAPbI_3$ films, since their deposition was better optimized than the $DMAPbI_3$.

6.3.1 Particle size of the precursor solutions

It was reported that, against what was initially believed, the precursor solutions were not perfect solutions, but colloidal suspensions[26]. This could be easily proved by observing the light dispersion due to the Tyndall effect of a laser beam passing through the solutions, as shown in **Figure 6.8**. When the laser beams passes through one of the solutions it is clearly visible. For comparison, it can be seen that no such thing happens when the laser passes through distilled water.

The particle size of the solutions with varying amounts of Chloride was measured, and the results for the four solutions are shown in **Figure 6.9**. The numbers *X-1-1* refer to the molar ratios of MACl, MAI and PbI_3 respectively. It can be seen that the amount of chloride has a clear and direct influence in the particle size of the solutions, as the sizes of the particles decrease as the amount of chloride present increases.

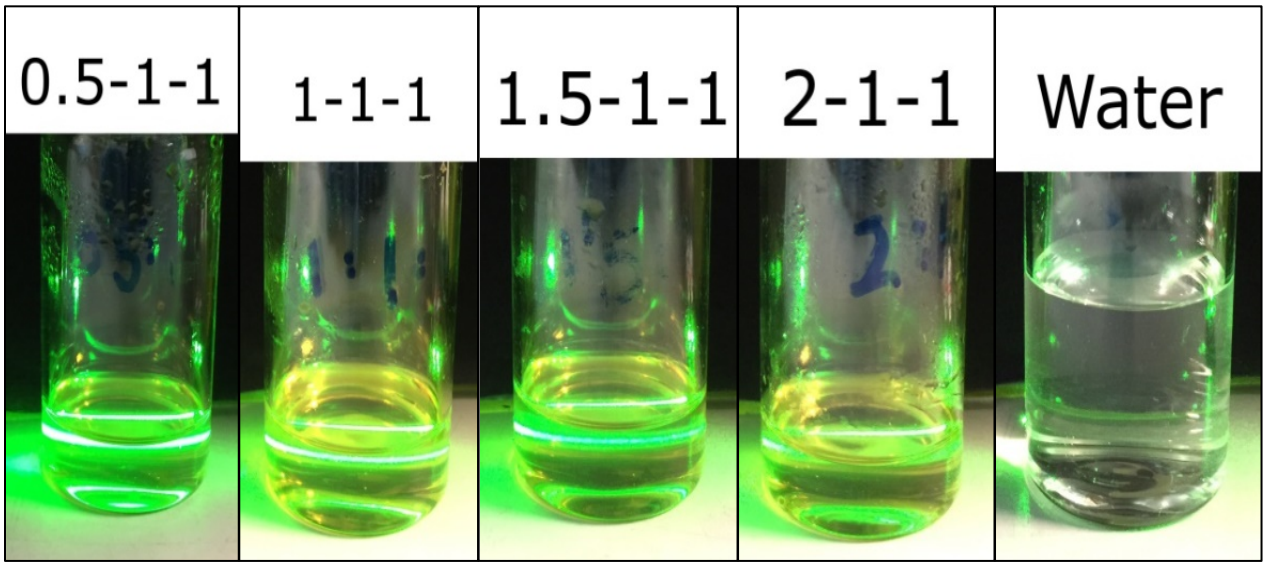

Figure 6.8

Tyndall effect in the precursor solutions

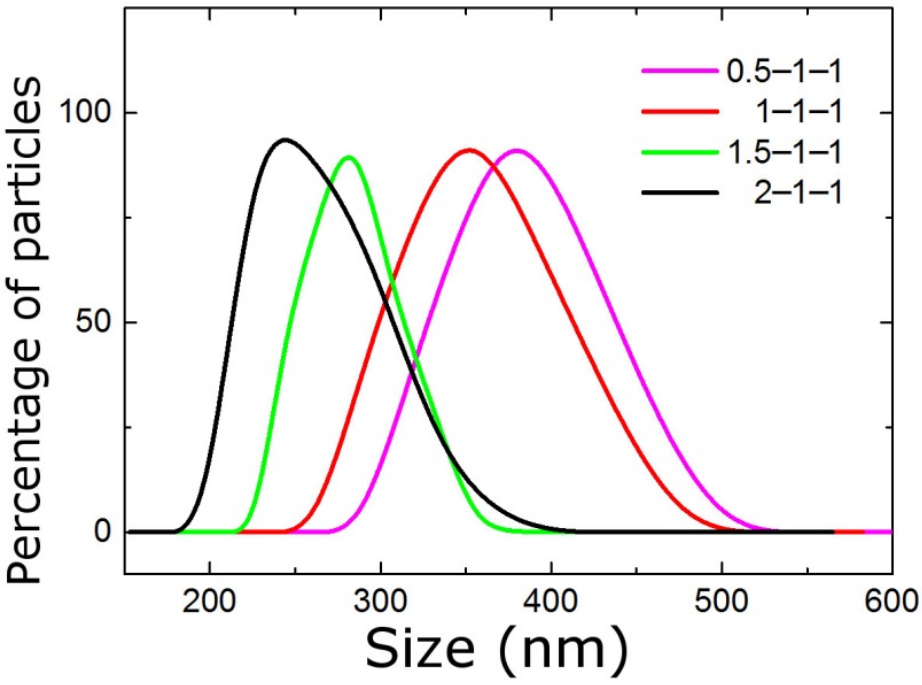

Figure 6.9

Particle size measuraments

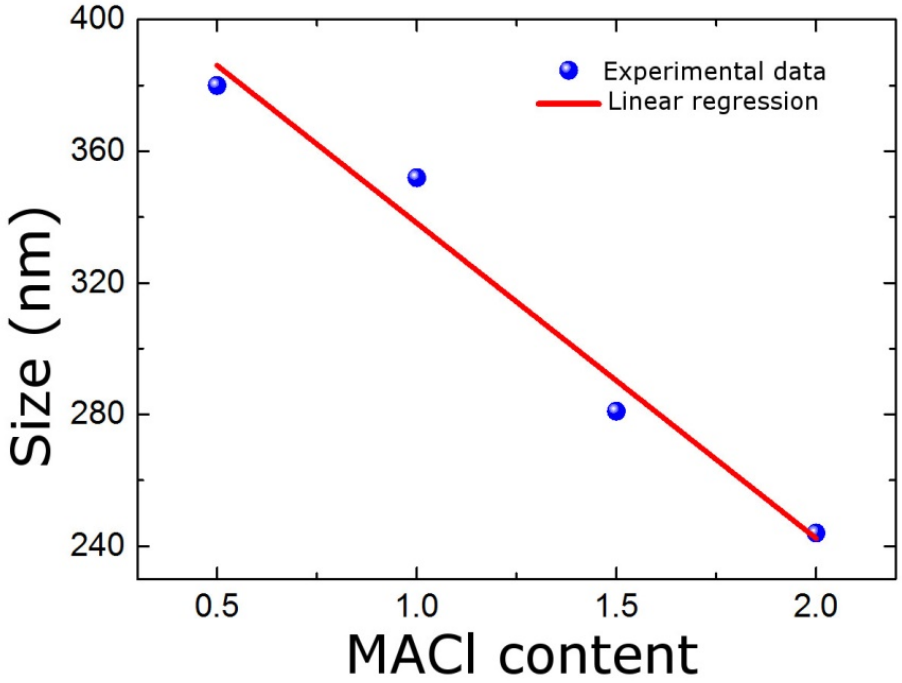

Figure 6.10

Relationship between particle size and MACl content

This can more clearly be seen in **Figure 6.10** where a linear correlation is observed between the MACl content and the most common size of the particles (peaks in the size distribution graph). An explanation of this effect was proposed by Keyou Yan *et al.*[26]:

- The PbI_2 crystallizes in a trigonal space group, with stacked planes made of $[PbI_6]$ octahedra along the *c*-direction. While the bonds within the planes are strong chemical bonds, the bonds between the planes are only weak Van der Waals forces.
- When in the PbI_2 is dissolved in DMF, the solvent is capable of breaking the weak bonds between the planes. Complete dissolution of the PbI_2 is achieved when also a few of the chemical bonds inside the planes are also broken.
- The organic compounds, CH_3NH_3X, are able to act as surfactants and to coordinate to the breakaway planes of PbI_2. As the organic component increases by adding MACl the dissolved PbI_2 is further stabilized.
- Higher concentrations of MACl allow for further dissolution of PbI_2, which losses its trigonal structure to enter a quasi-tetragonal soft framework more resembling the perovskite.

6.3.2 Influences in thin film morphology

It was also believed that the change in particle size of the precursor solutions could affect the final morphology of the thin films. To that end, thin films were prepared form each of the precursor solutions using the one-step deposition technique. The resulting films were observed under the SEM, and the resulting images are shown in **Figure 6.11**. As can be seen, higher amounts of chloride and therefore lower particle sizes led to a loss of the needle-like morphology towards a more homogeneous film. As explained earlier, this is due to the surfactant effect of the organic component of the precursor, which stabilizes a coordination complex for the PbI_2 in solution more resembling the final perovskite, avoiding the formation of needle structures. However, in most of the thin films the substrate was not properly covered, and the morphology was still not perfectly homogeneous, so some more optimization still has to be done.

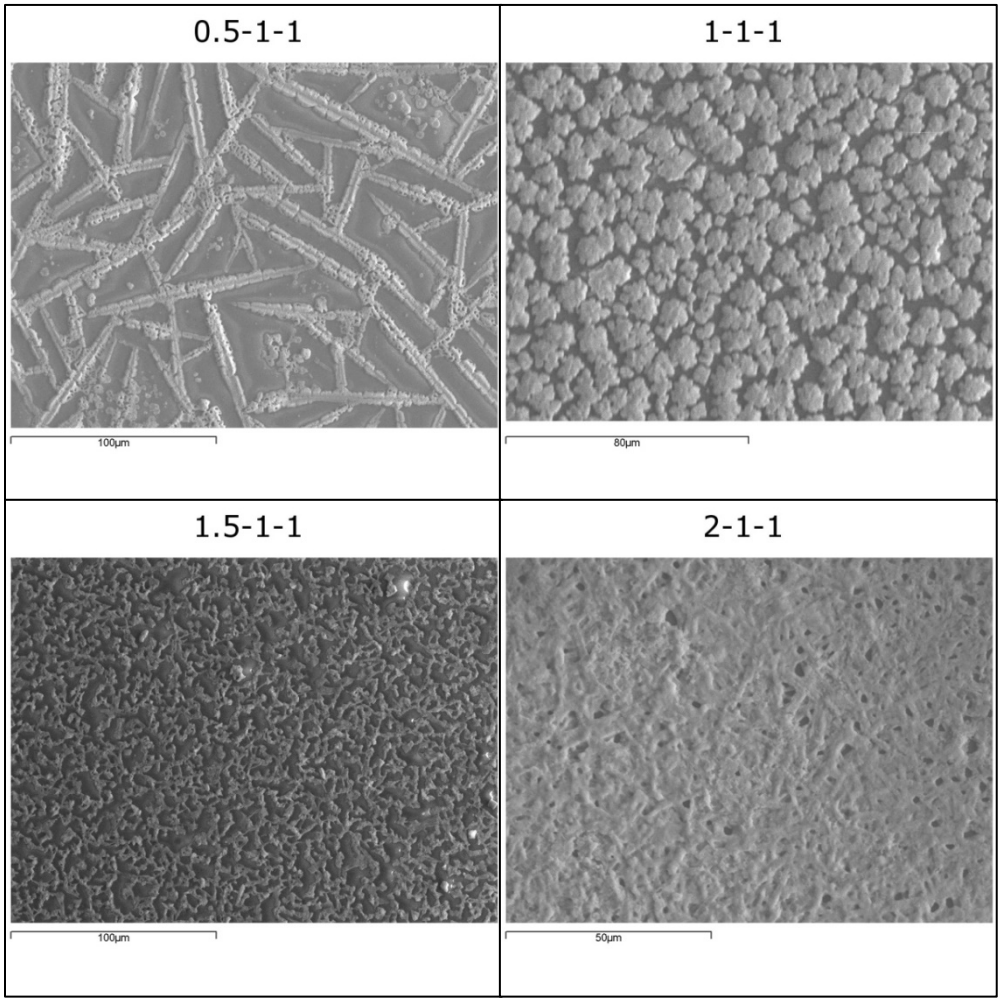

Figure 6.11

SEM images of thin films with X-1-1 MACl:MAI:PbI_2

6.3.3 Presence of Chloride

A final question that was answered was whether the Chloride itself would enter into the perovskite structure as an impurity or it would simply be eliminated during the thermal treatment. To that end, the thin films were analyzed using the Energy-dispersive X-ray spectroscopy (EDX) technique incorporated into the SEM that was being employed. This technique allows the X-rays generated by the electron beam interacting with the sample to be analyzed. Since each element emits X-rays of a specific energy, the technique allows individual elements to be identified within a sample. Also, an estimate of the concentration of the elements can also be obtained.

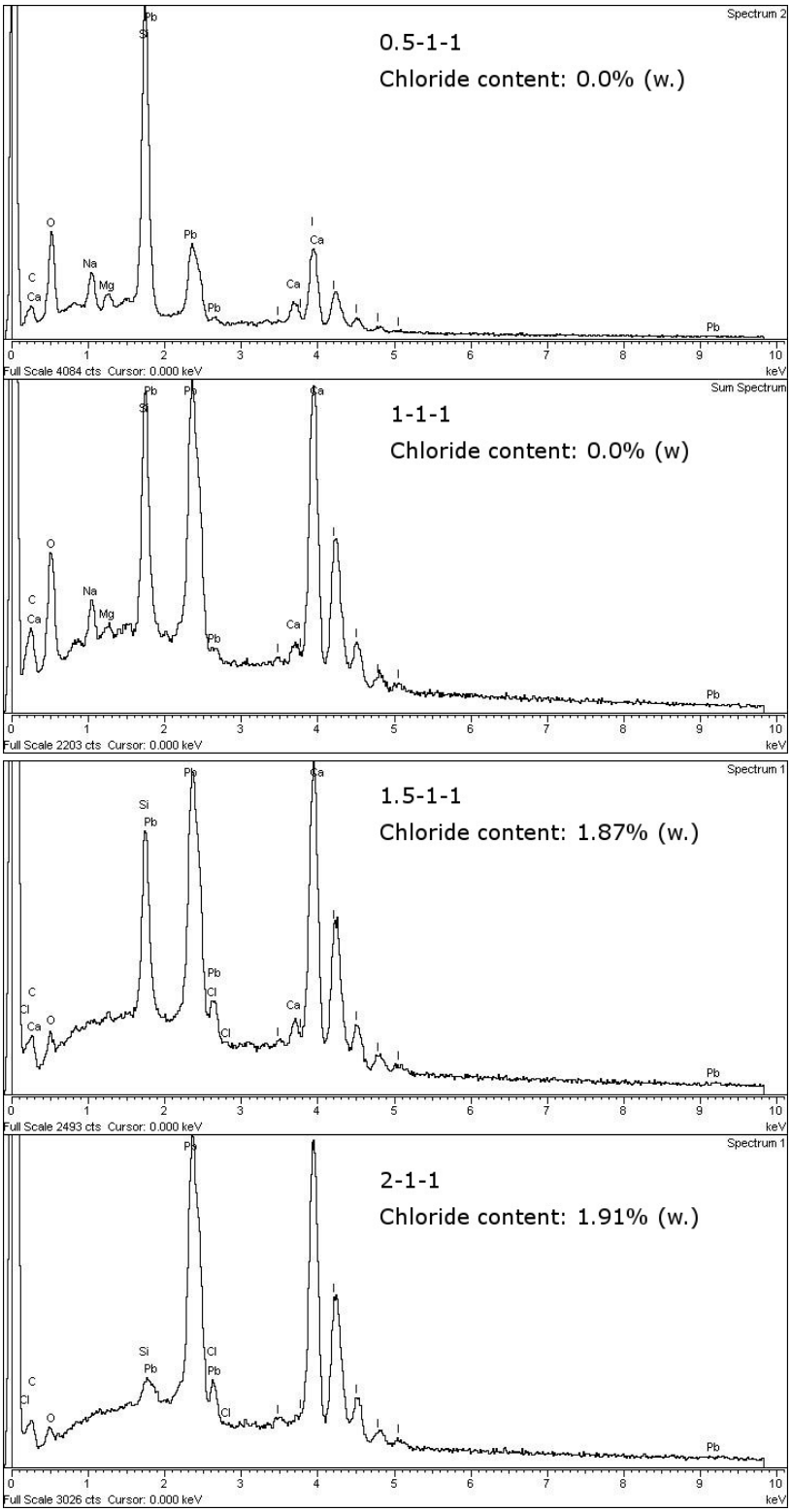

Figure 6.12

EDX spectra of the thin films

The results of this technique applied to the samples are shown in **Figure 6.12**. Only in the films with higher starting amount of chloride (1.5-1-1 and 2-1-1films) was present any chloride, and even so in small amounts. Regardless, it was proved that chloride is capable of entering the structure of thee perovskite.

It should also be noted that this small presence of chloride did not dramatically changed the optical properties of the compound. The electronic band gap was measured for those thin films, and the results are 1.60 eV for those films apparently without Cl (0.5-1-1 and 1-1-1 films) and 1.63 for those with small amounts of Cl (1.5-1-1 and 2-1-1 films). The introduction of small amounts of chloride could lead to a better fine-tuning of the perovskite, keeping its photovoltaic properties.

6.4 DMAX and MAX as additives in $DMAPbI_3$ precursor solutions

Since the particle size of the $DMAPbI_3$ precursor solution could not be measured, probably because it being too large and falling outside the range of the instrument, it was decided to use DMACl, MAI and MACl to reduce it.

6.4.1 Change in particle size

As can be seen in **Figure 6.13**, the particle size was successfully reduced, although not as much as when using MACl as additive. This could be blamed on the presence of DMA, which seems to be a worse surfactant than the MA. The size reduction is similar for all three samples, with the exception of the MACl:DMAI 1:1.5 solution, which has a larger particle size. These results support the theory explained above that is the organic compounds that act as a surfactant and help dissolve the PbI_2, since the size reduction still takes place, regardless of the organic compound used as additive. Despite this, the exact nature of the organic compound still has some effect, as well as the presence or absence of chloride.

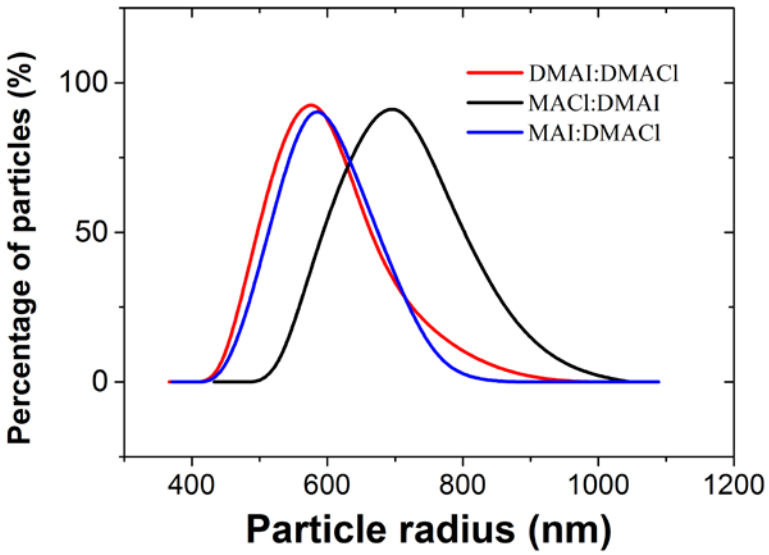

Figure 6.13

Particle size of the DMAX solutions

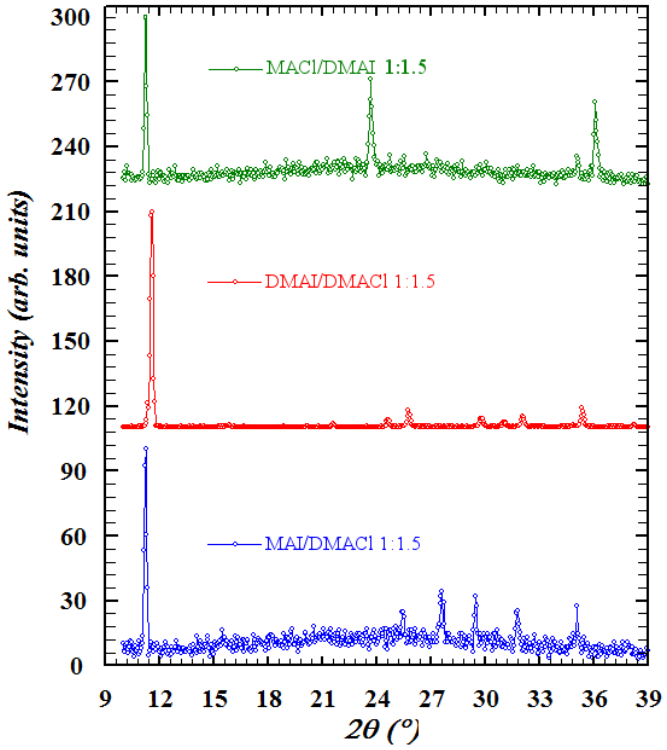

Figure 6.14

The XR-diffraction pattern of the MAI/DMACl, DMAI/DMACl and the MACl/DMAI thin films

6.4.2 Thin films

To check the effectiveness of using the additives, the precursor solutions were deposited. The films were sent to XRPR; and the resulting XR-diffraction patterns are shown in **Figure 6.14**. Despite the somewhat different composition, all three samples have a strong peak at $2\theta = 11°$. Only in the case DMAI/DMACl mixture is the peak a little offset. A closer look to that region, as in **Figure 6.15**, reveals that despite the presence of MA, sometimes in higher quantities, the compound retains the hexagonal perovskite crystal structure of the $DMAPbI_3$, instead of that of the $MAPbI_3$. This proves that MAX compounds can be used as additives in the preparation of $DMAPbI_3$ thin films, but not the other way around, since the compound formed will be $DMAPbI_3$. It should also be noted that the thin films obtained using additives are much pure than without them, as almost no PbI_2 impurities are left. Once again, this indicates a better solving of the PbI_2.

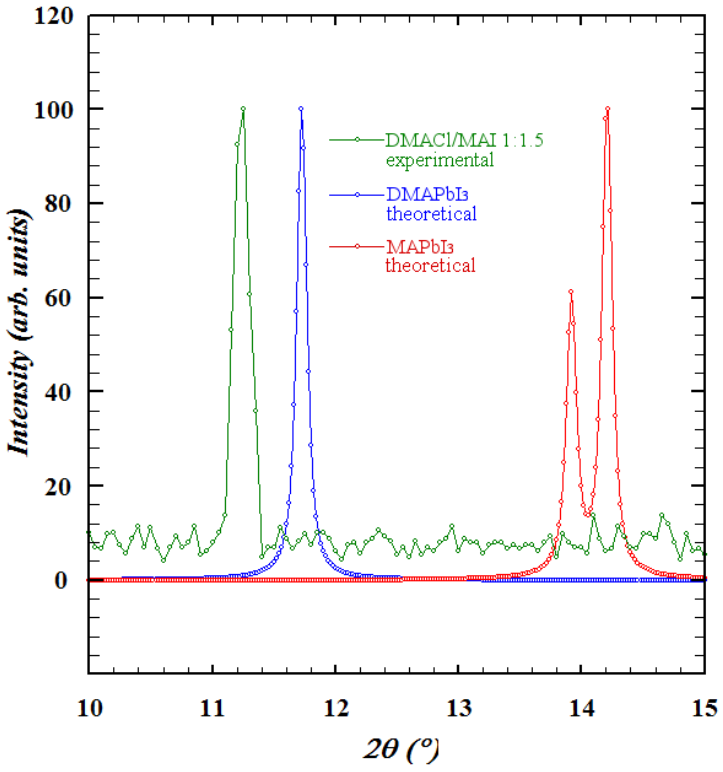

Figure 6.13

Detail of the XR-diffraction pattern of the DMACl/MAI sample

Finally, the SEM images obtained of the thin films, shown in **Figure 6.16**, proved that the additives were successful in avoiding the needle-like morphology, obtaining a more homogenous one. However, a good covering of the substrate was still not achieved, demonstrating the need for further optimization of the process.

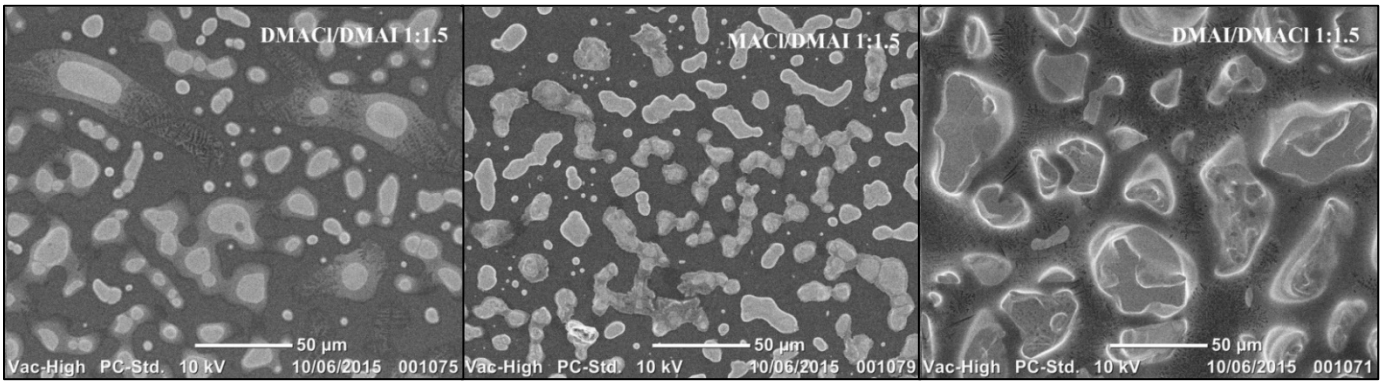

Figure 6.14

SEM images of the different thin films

7 CONCLUSIONS

7.1 English

Taking into account the above results and the accompanying discussion the following conclusions can be reached:

- The $DMAPbI_3$ was successfully obtained by first time in bulk by mixing the reagents, DMAI and PbI_2, a very simple method. Its crystal structure was proved to be that of a hexagonal perovskite. Comparison of its XR-diffraction pattern with its theoretical one proved beyond any doubt that the compound had been formed as a single phase.
- The optical properties of the $DMAPbI_3$ made it unsuitable for photovoltaic use, although the very same properties made it an interesting material for a blue LED design.
- A thin film of $DMAPbI_3$ was successfully synthetized by the one-step technique,. However, the obtained SEM images showed a non-homogeneous needle-like morphology.
- The thin film prepared by the two-step technique was also unsuitable for photovoltaic use. While small amounts of the perovskite were synthetized, there were still PbI_2 impurities and the substrate was only partially covered.
- When using the one or two steps techniques the thin films had large PbI_2 impurities. Those were avoided, however, when additives were employed.
- It was proved that the MACl could be successfully used as an additive to the precursor solutions of $MAPbI_3$. Those were indeed proven to be colloidal solutions by observing the Tyndall effect. Furthermore, it was shown that the size of those colloids was in clear inverse relationship with the amount of MACl in the solution. This was explained by the surfactant effect of the organic compounds in the solution.
- MAX and DMAX compounds could also be successfully used as additives to the $DMAPbI_3$ precursor solutions. They managed to reduce the particle size of the solu-

tions, while the $DMAPbI_3$ crystal structure remained in the deposited films with higher purity, despite the presence of MA.

- The particle size of the solutions also had an impact in the final morphology of the thin films. Better, more homogenous morphologies were obtained with smaller particle sizes. Also, it was proved that small amounts of chloride were capable of entering the perovskite structure.

7.2 Galego

Tendo en conta os resultados mostrados anteriormente, e a discusión dos mesmos, pódense achegar ás seguintes conclusións:

- O $DMAPbI_3$ foi sintetizado por primeira vez como mostra policristalina mediante un método moi sinxelo mesturando os reactivos DMAI e PbI_2. A súa estrutura cristalina é a dunha perovskita hexagonal. A comparación do seu patrón de difracción de raios-X demostrou sen lugar a dúbidas que o composto fora formado como unha fase pura.
- As propiedades do $DMAPbI_3$ fano inadecuado para usos fotovoltaicos, aínda que esas mesmas propiedades convérteno nun material interesante para un deseño dun LED azul.
- Unha capa fina de $DMAPbI_3$ foi satisfactoriamente sintetizada mediante o procedemento nun paso. Sen embargo, as imaxes obtidas mediante SEM mostraron una morfoloxía non homoxénea con forma de agullas.
- A capa fina preparada polo procedemento en dous pasos tamén era inadecuada para uso fotovoltaico. Se ben foron sintetizadas pequenas cantidades da perovskita, aínda había impurezas de PbI_2 e o substrato tan solo foi parcialmente recuberto.
- O empregarse a técnica en un o dous pasos, as capas depositadas tiñas impurezas de PbI_2. Sen embargo, estas evitáronse ao empregar aditivos.
- Probouse que o MACl podía ser empregado satisfactoriamente como aditivo nas disolucións precursoras de $MAPbI_3$. Probouse tamén que estas eran disolucións coloidais, ao observarse o efecto Tyndall. Ademais, mostrouse que o tamaño de eses coloides estaba nunha clara relación inversa coa cantidade de MACl na solución. Isto explícase polo efecto surfactante das especies orgánicas na solución.
- Compostos como MAX ou DMAX tamén foron empregados satisfactoriamente como aditivos para as solución precursoras de $DMAPbI_3$. Foron capaces de reducir o

tamaño de partícula das disolucións, mentres que a estrutura cristalina do $DMAPbI_3$ permanecía nas capas depositadas cunha maior pureza, a pesar da presenza de MA.

- O tamaño de partícula das disolucións tamén tivo un impacto na morfoloxía final das capas finas. Morfoloxías mellores e mais homoxéneas foron obtidas cun tamaño de partícula menor. Tamén probouse que pequenas cantidades de cloro eran capaces de introducirse na estrutura da perovskita.

7.3 Castellano

Teniendo en cuenta los resultados anteriores y la discusión de los mismos se pueden alcanzar las siguientes conclusiones:

- El compuesto $DMAPbI_3$ fue sintetizado por primera vez con un método muy sencillo mezclando los reactivos DMAI y PbI_2. Su estructura cristalina es la de una perovskita hexagonal. . La comparación de su patrón de difracción de rayos-X mostró sin lugar a dudas que el compuesto había sido formado como una fase pura.
- Una capa fina de $DMAPbI_3$ fue satisfactoriamente sintetizada mediante el procedimiento en un paso. Sin embargo, las imágenes de SEM obtenidas mostraron una morfología no homogénea y con formas de aguja.
- La capa fina preparada por el procedimiento en dos pasos también resultó ser inadecuada para uso fotovoltaico. Si bien pequeñas cantidades de perovskita fueron sintetizadas, había grandes impurezas de PbI_2, y el sustrato tan solo fue parcialmente recubierto.
- Al emplearse la técnica en uno o dos pasos, las capas finas tenían impurezas de PbI_2. Sin embargo, estas se evitaron al emplear aditivos.
- Se demostró que el MACl podía ser utilizado exitosamente como aditivo en las disoluciones precursoras de $MAPbI_3$. También se demostró que estas eran de hecho disoluciones coloidales al observarse el efecto Tyndall. Además se mostró que el tamaño de estos coloides estaba en una relación clara e inversa con la cantidad de MACl en la disolución. Esto se explica por el efecto surfactante de los compuestos orgánicos en la solución.
- Compuestos de tipo MAX y DMAX también se emplearon satisfactoriamente como aditivos a las disoluciones de $DMAPbI_3$. Fueron capaces de reducir el tamaño de partícula de las disoluciones, mientras que la estructura cristalina del $DMAPbI_3$ era mantenida en las capas depositadas con una mayor pureza, pese a la presencia de MA.

- El tamaño de partícula de las disoluciones también tenía un impacto en la morfología final de las capas finas. Morfologías mejores y más homogéneas fueron obtenidas con un tamaño de partícula más pequeño. También se probó que pequeñas cantidades de Cloro eran capaz de introducirse en la estructura de la perovskita.

8 BIBLIOGRAPHY

1. Cook J, Nuccitelli D, Green SA, et al. Quantifying the consensus on anthropogenic global warming in the scientific literature. *Environmental Research Letters*. 2013;8(2):024024.

2. D. Callister W, G. Rethwisch D. *Materials science and technology.* Eighth Edition ed. John Wiley & Sons; 2011; 978-0-470-50586-1.

3. Atkins PW. *Physical Chemistry.* Fifth Edition ed. Oxford University Press; 1994.

4. D. Fahlman B. *Materials Chemistry.* Second Edition ed. Springer; 2011; 978-94-007-0692-4.

5. Grupo FerroAtlantica. SiMe photovoltaic solar quality. http://www.ferroatlantica.es/index.php/en/solar-fotovoltaica/division-fotovoltaica. Accessed 08/09, 2015.

6. Zuser A, Rechberger H. Considerations of resource availability in technology development strategies: The case study of photovoltaics. *Resour Conserv Recycling*. 2011;56(1):56-65.

7. Docampo P, Guldin S, Leijtens T, Nakita K. N, Steiner U, J. Snaith H. Lessons learned: From dye-senstized solar cells to all-solid-state hybrid devices. *Advanced Materials*. 2014;10.

8. Moser J. Note about the gain photoelectric currents by optical sensitization. *Monatsh.Chem*. 1887;8:373.

9. Namba S, Hishiki Y. Color sensitization of zinc oxide with cyanine Dyes1. *J Phys Chem*. 1965;69(3):774-779.

10. O'regan B, Grätzel M. A low-cost, high-efficiency solar cell based on dye-sensitized colloidal TiO2 films. *Nature*. 1991;353(6346):737-740.

11. Snaith HJ. Estimating the maximum attainable efficiency in dye-sensitized solar cells. *Advanced Functional Materials*. 2010;20(1):13-19.

12. Bach U, Lupo D, Comte P, et al. Solid-state dye-sensitized mesoporous TiO2 solar cells with high photon-to-electron conversion efficiencies. *Nature*. 1998;395(6702):583-585.

13. Kroeze J., Hirata N., Schmidt-Mende L., et al. Parameters influencing charge separation in solid-state dye-sensitized solar cells using novel hole conductors. *Advanced Functional Materials*. 2006;16(14):1832-1838.

14. Sun J, Goldys EM. Linear absorption and molar extinction coefficients in direct semi-conductor quantum dots. *J. Phys. Chem. C*. 2008;112(25):9261-9266.

15. Kojima A, Teshima K, Shirai Y, Miyasaka T. Organometal halide perovskites as visi-ble-light sensitizers for photovoltaic cells. *J. Am. Chem. Soc*. 2009;131(17):6050-6051.

16. Kim H, Lee C, Im J, et al. Lead iodide perovskite sensitized all-solid-state submicron thin film mesoscopic solar cell with efficiency exceeding 9%. *Scientific Reports*. 2012;2:591.

17. Laban WA, Etgar L. Depleted hole conductor-free lead halide iodide heterojunction solar cells. *Energy Environ Sci*. 2013;6(11):3249-3253.

18. Kazim S, Khaja Nazeeruddin M, Grätzel M, Ahmad S. Perovskite as light harvester: A game changer in photovoltaics. *Angewandte Chemie International Edition*. 2014;53:2812-2812-2824.

19. Zheng L, Zhang D, Ma Y, et al. Morphology control of the perovskite films for efficient solar cells. *Dalton Trans*. 2015;44(23):10582-10593.

20. Wells AF. *Structural Inorganic Chemistry.* Fifth Edition ed. Oxford: Clarendon Press; 1984.

21. Cheng Z, Lin J. Layered organic–inorganic hybrid perovskites: Structure, optical properties, film preparation, patterning and templating engineering. *CrystEngComm*. 2010;12(10):2646-2662.

22. R. West A. *Solid State Chemistry and its Applications.* Second Edition ed. John Wiley & Sons, Ldt; 2014.

23. Baikie T, Fang Y, M. Kadro J, et al. Synthesis and crystal chemistry of the hybrid perovskite $(CH_3NH_3)PbI_3$ for solid-state sensitised solar cell aplications. *Journals of Materials Chemistry A*. 2013;1:5628-5628-5641.

24. - Im J, - Lee C, - Lee J, - Park S, - Park N. - 6.5% efficient perovskite quantum-dot-sensitized solar cell. - *Nanoscale*. (- 10):- 4088.

25. Jeong-Hyeok I, Hui-Seon K, Nam-Gyu P. Morphology-photovoltaic property correlation in perovskite solar cells: One-step deposition of $CH_3NH_3PbI_3$. *APL Materials*. 2014;2.

26. Keyou Yan, Mingzhu Long, Tiankai Zhang, et al. Hybrid halide perovskite solar cell precursors: Colloidal chemistry and coordination engineering behind device processisng for high effinciency. *Journal of the American Chemical Society*. 2015.

27. Giacovazzo C, Monaco HL, Artioli G, et al. *Fundamentals of crystallography*. Oxford Science Publications; 2002.

28. Servicios de Apoio a Investigación. Servicios de apoio a investigación: Análisis estructural: Equipamento. https://www.sai.udc.es/es/unidades/UAE/equipamiento. Accessed 09/10, 2015.

29. Servicios de Apoio a Investigación. Servicios de apoio a investigación: Microscopia: Equipamento. https://www.sai.udc.es/gl/unidades/UM/equipamiento. Accessed 09/09, 2015.

30. Skoog DA, Holler FJ, Crouch SR. *Principios de análisis instrumental*. Sexta Edición ed. Santa Fe, Mexico: Cengage Learning; 2008.

31. Autralian microscopy & microanalysis research facility. what is a SEM (parts of the machine)? http://www.ammrf.org.au/myscope/sem/background/whatissem/. Accessed 07/30, 2015.